

# The phases and amplitudes of gravity waves propagating and dissipating in the thermosphere: Application to measurements over Alaska

M. J. Nicolls,<sup>1</sup> S. L. Vadas,<sup>2</sup> J. W. Meriwether,<sup>3</sup> M. G. Conde,<sup>4</sup> and D. Hampton<sup>4</sup>

Received 18 January 2012; revised 21 March 2012; accepted 3 April 2012; published 23 May 2012.

[1] In a companion paper, we derived the high-frequency, compressible, dissipative polarization relations for gravity waves (GWs) propagating in the thermosphere. In this paper, we apply the results to nighttime thermospheric observations of a GW over Alaska on 9–10 January 2010. Using a vertically-pointed Fabry-Perot interferometer (FPI) at Poker Flat that measured vertical wind perturbations ( $w'$ ) and two FPIs that measured the line-of-sight (LOS) velocities in four common volumes, we inferred a GW ground-based period  $\sim 32.7 \pm 0.3$  min, horizontal wavelength  $\lambda_H = 1094 \pm 408$  km, horizontal ground-based phase speed  $c_H \sim 560 \pm 210$  m/s, and propagation azimuth  $\theta \sim 33.5 \pm 15.8^\circ$  east-of-north. We compared the phase shifts and amplitude ratios of this GW with that predicted by the GW dissipative polarization relations derived in the companion paper, enabled by the ability of the FPIs to measure fundamental GW parameters (wind and temperature perturbations). We find that GWs with  $\lambda_H \sim 700$ – $1100$  km,  $\lambda_z \sim -500$  to  $-350$  km,  $\theta \sim 15$  to  $50^\circ$ , and  $c_H \sim 350$ – $560$  m/s agree with the observations if the primary contribution to the 630-nm emission was near the upper portion of that layer. The source of GW was likely thermospheric given the large intrinsic phase speed of the wave. Possible sources are discussed, the most likely of which are related to the onset of auroral activity near the time that the wave was initially observed.

**Citation:** Nicolls, M. J., S. L. Vadas, J. W. Meriwether, M. G. Conde, and D. Hampton (2012), The phases and amplitudes of gravity waves propagating and dissipating in the thermosphere: Application to measurements over Alaska, *J. Geophys. Res.*, *117*, A05323, doi:10.1029/2012JA017542.

## 1. Introduction

[2] Gravity waves (GWs) are ubiquitous in the thermosphere [e.g., *Bristow et al.*, 1996; *Djuth et al.*, 1997, 2004; *Oliver et al.*, 1997]. (Here, by GW, we refer to acoustic gravity waves [*Hines*, 1960].) Increasing observational and modeling evidence suggests that some GWs generated in the lower atmosphere (e.g., from deep convection, mountain wave breaking, weather fronts) may propagate into the thermosphere, where they eventually dissipate [*Bauer*, 1958; *Georges*, 1968; *Roettger*, 1977; *Hung and Kuo*, 1978; *Waldock and Jones*, 1987; *Kelley*, 1997; *Hocke and Tsuda*,

2001; *Bishop et al.*, 2006; *Vadas and Nicolls*, 2009]. Although this dissipation altitude depends sensitively on the vertical wavelength,  $\lambda_z$ , and the background temperature,  $\bar{T}$ , most GWs from the lower atmosphere dissipate below  $z < \sim 300$  km [*Vadas*, 2007; *Fritts and Vadas*, 2008]. The momentum deposited during the dissipation of these GWs excites secondary/tertiary GWs [*Vadas and Liu*, 2009, 2011]. These secondary/tertiary GWs can propagate to altitudes of 300–500 km before dissipating because of their large intrinsic frequencies, phase speeds, and vertical wavelengths [*Vadas*, 2007]. GWs are also excited at high latitudes in the thermosphere by Joule heating, particle precipitation, and the Lorentz forcing that accompanies the rapidly-evolving aurora [e.g., *Chimonas and Hines*, 1970; *Chimonas and Peltier*, 1970; *Francis*, 1973; *Walterscheid et al.*, 1985; *Mayr et al.*, 1984a, 1984b, 1987, 1990; *Hocke and Schlegel*, 1996; *Herrero et al.*, 1984]. These GWs can also propagate to 300–500 km before dissipating [*Richmond*, 1978; *Hajkowicz*, 1990; *Tsugawa et al.*, 2003; *Nicolls et al.*, 2004; *Ford et al.*, 2006, 2008; *Bruinsma and Forbes*, 2009].

[3] Fabry-Perot interferometers (FPIs) routinely measure the neutral wind in the auroral thermosphere using the 630-nm OI line. The emission layer may extend from 200–300 km altitude and is generated by particle impact. During soft particle precipitation events, the centroid altitude is typically

<sup>1</sup>Center for Geospace Studies, SRI International, Menlo Park, California, USA.

<sup>2</sup>CORA Division, NWRA, Boulder, Colorado, USA.

<sup>3</sup>Department of Physics and Astronomy, Clemson University, Clemson, South Carolina, USA.

<sup>4</sup>Geophysical Institute, University of Alaska Fairbanks, Fairbanks, Alaska, USA.

Corresponding author: M. J. Nicolls, Center for Geospace Studies, SRI International, 333 Ravenswood Ave., Menlo Park, CA 94025, USA. (michael.nicolls@sri.com)

**Table 1.** FPI Site Locations

Location	Latitude (°N)	Longitude (°E)
Poker Flat (PKR and PKZ)	65.118	−147.433
Fort Yukon (FYU)	66.560	−145.214

located near 240–250 km with the exact altitude dependent upon the characteristic energy of the soft particle flux. In the absence of soft particle precipitation, the 630-nm nightglow emission is much weaker but is located in the same altitude range or slightly higher. Because of relatively large errors ( $10\text{--}25\text{ ms}^{-1}$ ) arising from the use of a photomultiplier as the detector, the emphasis of these instruments has been on the horizontal neutral winds [e.g., *Nagy et al.*, 1974; *Sica et al.*, 1986a, 1986b], with only a few studies focussing on the vertical neutral wind [e.g., *Aruliah and Rees*, 1995; *Innis et al.*, 1997; *Smith*, 1998].

[4] Errors in line-of-sight (LOS) wind determination have decreased significantly with the switch to imaging CCD detectors in recent years [*Aruliah et al.*, 2005; *Ford et al.*, 2006, 2008; *Meriwether et al.*, 2011; *Makela et al.*, 2011]. The advantage of these imaging FPI observations over imaging all-sky FPI observations [e.g., *Conde and Smith*, 1995; *Conde et al.*, 2001; *Aruliah et al.*, 2010] during times of auroral activity is the ability to detect small Doppler shifts with errors of only several  $\text{ms}^{-1}$  in a given direction. The field-of-view (FOV) of FPI observations of the thermospheric region is narrow, typically  $\sim 1^\circ$ . Thus, the 630-nm Doppler shift is observed over a spatial extent of 4–5 km, minimizing the extent of any horizontal spatial averaging of the GW event observed. For these systems, the error for a Doppler shift measurement may be as small as  $1\text{--}3\text{ ms}^{-1}$  for an exposure time of 90 s, and the detection of GW wind fluctuations is readily possible when the emission intensity is high. As we demonstrate in this paper, a set of several FPIs which observe multiple common volumes in sequence can then enable the determination of the horizontal wavelength and direction of propagation of an observed GW.

[5] Because the altitudinal thickness of the nightglow OI 630-nm emission is 75–100 km, GWs with  $|\lambda_z| \ll 100\text{ km}$  may be difficult to detect. In particular, this effect reduces sensitivity to GWs from common lower atmospheric sources such as deep convective plumes and wave breaking near the mesopause (except those with  $|\lambda_z| > 100\text{ km}$  that have relatively small amplitudes) [*Vadas et al.*, 2003, 2009; *Fritts and Alexander*, 2003]. However, many aurorally-generated and secondary/tertiary GWs have  $|\lambda_z| > 100\text{ km}$ , thereby allowing for their detection by FPI systems. Although FPIs can observe these GWs, they cannot directly measure their vertical wavelengths. Yet a GW can only be reverse ray-traced accurately (for source identification) if all three components of a GW's wave vector is known. A method to infer  $\lambda_z$  from FPI measurements would therefore be beneficial for GW source studies. Such a method is described in our companion paper, and involves the measurement of the phase shifts and amplitude ratios of the components of observed GWs (such as horizontal/vertical winds and temperatures) [*Vadas and Nicolls*, 2012, hereinafter VN2012]. In that paper, we derive the full, compressible polarization relations for high-frequency GWs (with periods less than a few hours) which dissipate from kinematic viscosity and thermal diffusivity in the thermosphere. We then show that

the phase shifts and amplitude ratios of the GW components depend sensitively and uniquely on  $\lambda_H$ ,  $\lambda_z$ , the GW's intrinsic frequency, and the background parameters at the measurement altitude (such as the kinematic viscosity, buoyancy period, and density scale height).

[6] In section 2, we obtain the parameters for a GW observed on 9–10 January 2010 using observations from three FPIs, an all-sky imaging Fabry-Perot Spectrometer (the Poker Flat Scanning Doppler Imager, or SDI, which will be described in section 2.5), and the Poker Flat Incoherent Scatter Radar (PFISR). Section 3 compares the phase shifts and amplitude ratios associated with the GW polarization relations (derived in VN2012) with these observations. Section 4 contains a discussion of possible GW sources, and section 5 contains our conclusions.

## 2. Observations of a Gravity Wave on 9–10 January 2010 in Alaska

### 2.1. Observational Setup and Geometry of FPIs

[7] The imaging FPI neutral wind and temperature measurements reported in this paper were obtained with a network of three Fabry-Perot observatories located at the Davis Science Center at Poker Flat (which will be referred to as PKZ and PKR) and the Geophysical Institute Optical Observatory in Fort Yukon (which will be referred to as FYU). The latitudes and longitudes of these sites are given in Table 1. Data from the fourth Fabry-Perot observatory in Eagle, Alaska that allow for tri-static measurements were not available. PKZ measured the neutral vertical wind and temperature directly over Poker Flat in 90 s exposures. Every 10 exposures, a dark (D) and laser (L) image were obtained for calibration purposes. PKR and FYU measured the LOS neutral winds at 4 roughly common-volume (CV) regions east of Poker Flat and south of Fort Yukon. A two-axis steerable periscope was used to observe these CV regions and maintain the pointing accuracy to  $\sim 0.1^\circ$ . An observing sequence of CV1, CV2, CV3, and CV4, Z (zenith), D, and L required a cadence of 8.5 min. The geometry of these observations is shown in Figure 1.

[8] The optical characteristics of PKZ and FYU were similar. The spacer gap was 1.5 cm, the number of rings per image was 5 for FYU and 3 for PKZ. PKR had an aperture of 10 cm and an etalon with a 1-cm gap separation. The apertures for PKZ and FYU were 7 cm and 10 cm, respectively. The detector for each FPI was a back-thinned CCD detector with a quantum efficiency at 630 nm of  $\sim 90\%$ . The dark noise level was negligible at  $\sim 0.0005$  counts per pixel per second.

[9] The analysis of the images is described in *Meriwether et al.* [2011] and *Makela et al.* [2011]. Each image ring center was determined so that the one-dimensional interferogram could be computed by breaking up each image into equal-area annuli. Typically, the number of annuli per image was 500 for PKZ and FYU. The number of annuli was 200 for PKR, which had only one order. These interferograms were fit by a four-parameter model using a non-linear least squares fitting process to determine the best estimation of the Doppler line center, the Doppler width, the area, and the continuum background. The Doppler shift was inferred by comparison of the Doppler line center with a zenith reference. For PKZ, the zenith reference was based upon the laser image observations. The line center positions of these laser interferograms were shifted by a constant offset to adjust for

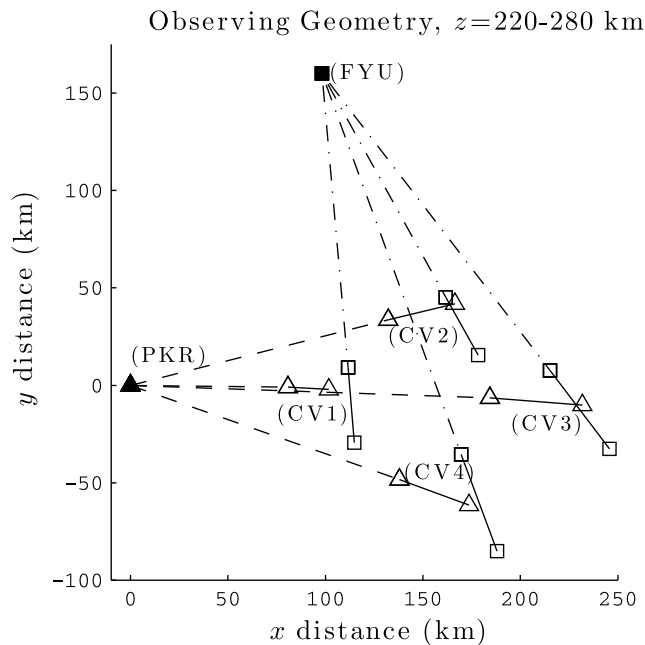


**Figure 1.** Observing geometry relative to Poker Flat (PKR) for bistatic FPI measurements from PKR and Fort Yukon (FYU) at four different  $\sim$ common volumes (CV1–CV4). Triangles (squares) denote PKR (FYU) observing locations at the heights of 220 km and 280 km that are connected by solid lines to show the possible range of 630-nm emission.

the phase difference between the laser line center and the 630-nm line center. This offset was determined by averaging all of the offsets between the zenith and the laser line centers using the assumption that the averaged zenith wind over the entire night was zero. With this procedure, an accurate estimate of the zenith reference was obtained. The Doppler stability for PKZ was excellent, with a drift of  $\sim 10$ – $20 \text{ ms}^{-1}$  over 15 h. The stability for FYU and PKR was  $\sim 100$ – $150 \text{ ms}^{-1}$  over 10–15 h.

[10] The vertical wind for PKZ and the LOS winds for PKR and FYU was computed by subtracting the zenith reference from the line center positions. The measurement error depended on the auroral 630-nm intensity. During quiet periods, the source emission is dominated by the 630-nm nightglow, and the measurement error typically varies between  $5$ – $10 \text{ ms}^{-1}$ . During active auroral conditions, the measurement error can be as small as  $\sim 1$ – $2 \text{ ms}^{-1}$  for a source emission of 500 R to 5 kR. These LOS Doppler shift measurements represent a weighted average of the thermospheric wind from 200–225 to 275–300 km altitude, which represents the vertical extent of the auroral 630-nm emission layer. The same altitude limits apply to the 630-nm nightglow layer. The neutral background wind within this altitude range is believed to be relatively constant because the viscosity of the fluid is sufficiently high to remove significant altitude gradients [Rishbeth, 1972].

## 2.2. FPI Vertical Winds and Temperatures

[11] The FPI observatory operated during the nighttime in January 2010. Many nights showed indications of wave activity. On 9–10 January, strong “monochromatic” wave structure was observed. Although some soft particle

precipitation was observed and there was a significant increase in the 630-nm emission (Figure 2a), the aurora was not especially active this night. Figure 2b shows the measured vertical velocity and temperature perturbations from 2500–2900 LT (LT = UT-9 h), where the averaged value from 2630 to 2800 LT has been subtracted. The average temperature and vertical velocities during this time period were  $\bar{T} \approx 636 \text{ K}$  and  $\bar{w} \approx 18 \text{ m/s}$ . Note that the error bars on the temperature measurements were smallest when the signal intensity is large from 2630 to 2800 LT. Correlated, monochromatic oscillations in both  $T$  and  $w$  were clearly visible from 2600 to 2830 LT. These periodic fluctuations were seen superimposed upon a long-period wave structure with upward wind during the period of auroral activity (26–28 LT) of  $\sim 15$ – $20 \text{ ms}^{-1}$  that were preceded by a period of downward wind of  $\sim 25$ – $30 \text{ ms}^{-1}$  near 20 LT. This form of a long-period downward and upward vertical wind structure observed in conjunction with auroral activity that appeared during the period of upward motion has been reported elsewhere [Aruliah and Rees, 1995; Innis et al., 1997; Smith, 1998], and will not be discussed further here. The wave period of the monochromatic wave series was seen to be  $\tau_r \approx 32 \text{ min}$ . Although there was considerable uncertainty and variability, the temperature perturbations led the vertical velocity perturbations by  $\sim 80^\circ$ , and had amplitudes of  $T' \approx 17 \text{ K}$  and  $w' \approx 15 \text{ m/s}$ .

## 2.3. FPI LOS Winds, and Deduced Background Winds

[12] We utilize the LOS winds from PKR and FYU to resolve the winds at the CV locations. A given LOS wind measurement  $i$  corresponds to,

$$U_i = Ua_e + Va_n + Wa_z \quad (1)$$

where  $(U, V, W)$  is the neutral wind vector and

$$\hat{\mathbf{a}} = (a_e, a_n, a_z) = (\cos \theta \sin \phi, \cos \theta \cos \phi, \sin \theta) \quad (2)$$

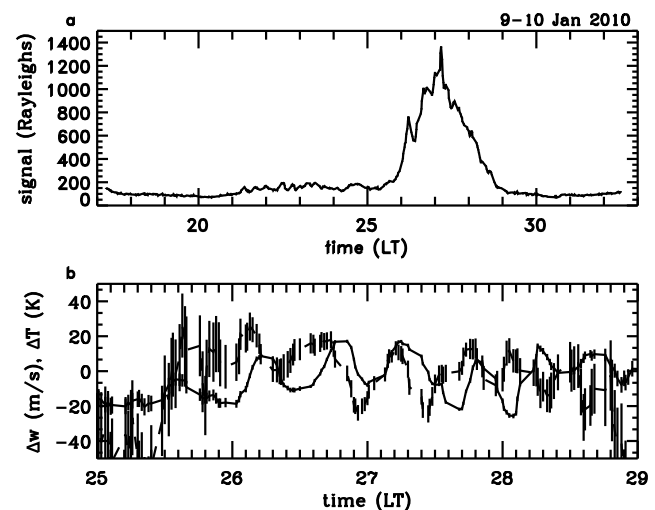


**Figure 2.** PKZ measurements on the night of 9–10 January 2010. (a) Signal (in Rayleighs). (b)  $w - \bar{w}$  (in m/s) (solid line) and  $T - \bar{T}$  (in K) (dashed line) smoothed with a 5-point running average.  $\bar{w} = 18 \text{ m/s}$  and  $\bar{T} = 636 \text{ K}$  are averages from 2630 to 2800 LT. The error bars are shown by solid lines.

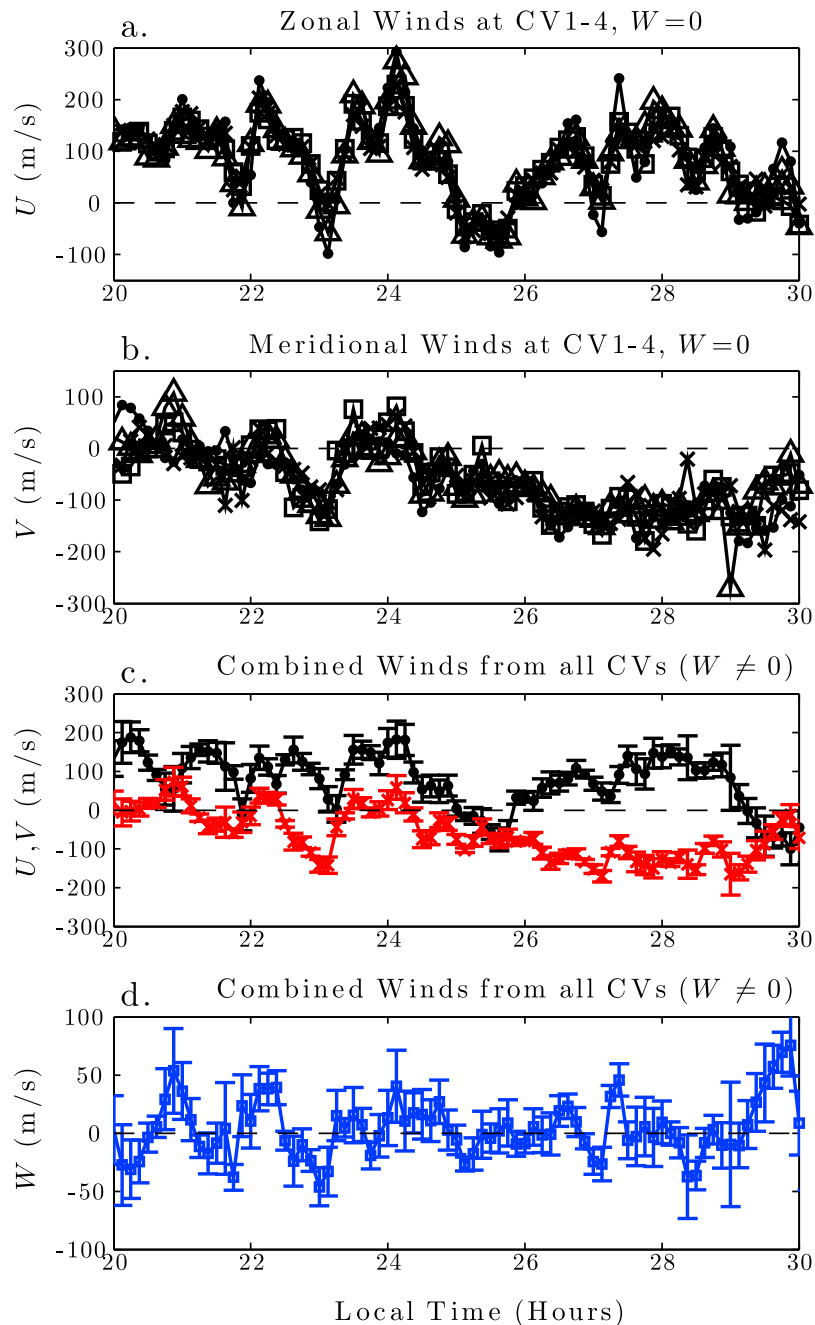


**Figure 3.** (a, b) Zonal and meridional winds, respectively, computed at all four CVs (each denoted with a different symbol) assuming  $W = 0$ . (c, d) Average background winds, assuming the winds are uniform over the entire region. Figure 3c shows  $U$  (black),  $V$  (red), and Figure 3d shows  $W$  (blue) obtained by combining LOS measurements from all CVs.

for a look-direction at azimuth  $\phi$  and elevation angle  $\theta$ . The subscripts “e”, “n”, and “z” refer to eastward, northward, and vertical directions, respectively. To get a general understanding of the consistency of the measurements for the 4 CVs, we first assume that the vertical wind,  $W$ , is negligible (this assumption will be relaxed shortly). Then the two measurements at each CV can be used to determine  $U$  and  $V$ . The resulting  $U$  and  $V$  for each CV are shown in Figures 3a and 3b. The winds are generally consistent from CV to CV, and are generally southeastward and relatively uniform for the post-midnight period from  $\sim 2630$ –2800 LT.

This suggests that the background vertical winds are significantly smaller than the horizontal winds.

[13] We now calculate the background, mean  $U$ ,  $V$ , and  $W$  winds over the entire volume. We assume that these background winds are spatially uniform over the entire region, and use the 8 LOS measurements at each time  $t$  to resolve averaged  $U$ ,  $V$ , and  $W$ . (Note that with 3 unknowns and 8 measurements, the solution is overdetermined.) These background winds do not include the wind components of the GWs, which will be inferred from the measurements in the next section. This approach

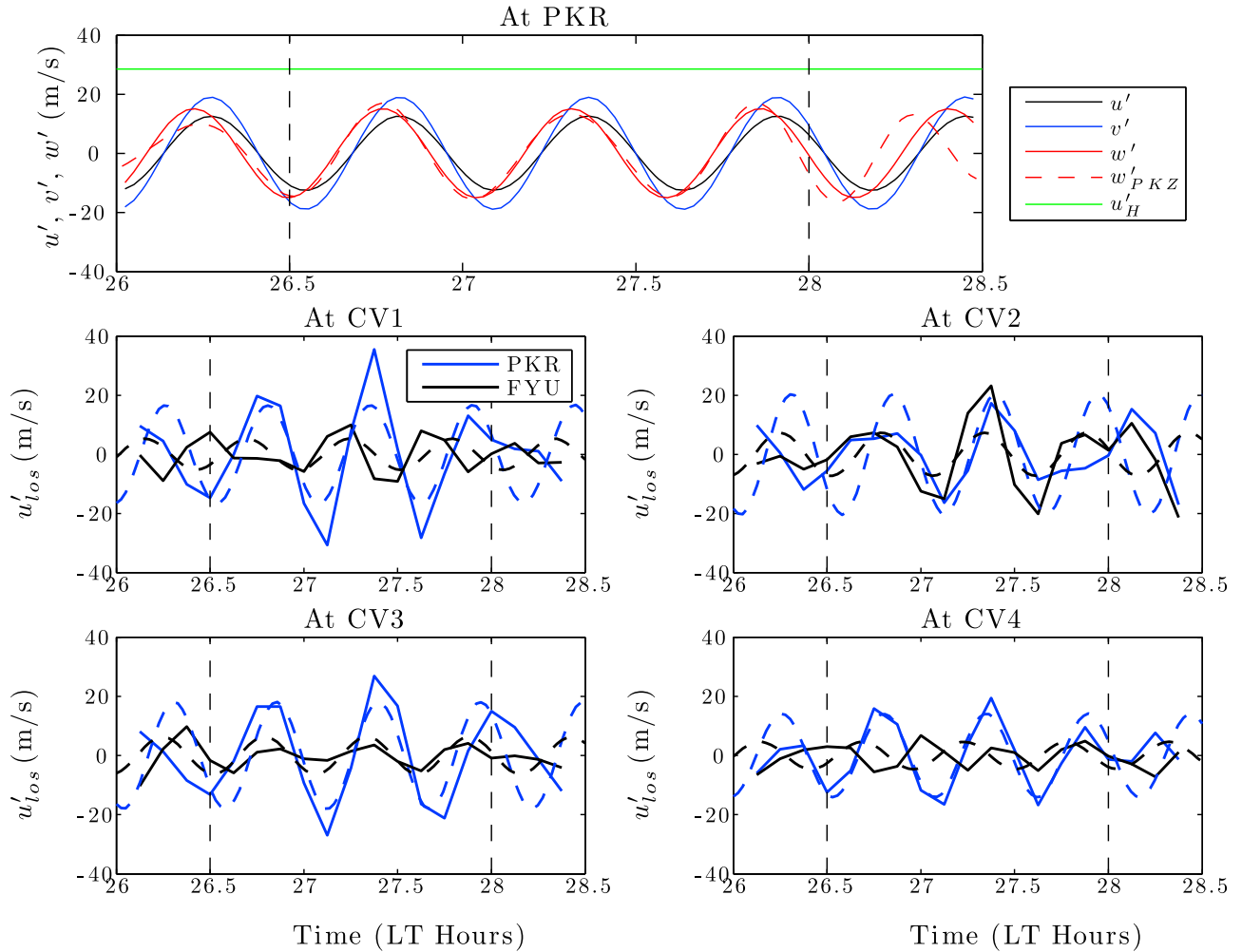


**Figure 4.** (top) Forward model results at the location of Poker Flat:  $u'$  (black solid),  $v'$  (blue solid),  $w'$  (red solid), and derived GW horizontal velocity amplitude  $u'_{H0}$  (green solid). We also show the measured, filtered vertical velocity (red dashed). (middle and bottom) Forward model results (dashed) and measurements (solid) of the LOS velocities at all four CVs from PKR (blue) and FYU (black). The errors on LOS velocity measurements were assumed to be  $\sim 7.5$  m/s, including geophysical variation.

can be expressed in matrix form as [e.g., Nicolls *et al.*, 2010]

$$\begin{pmatrix} U_1 \\ U_2 \\ \vdots \\ U_8 \end{pmatrix} = \begin{pmatrix} a_e^1 & a_n^1 & a_z^1 \\ a_e^2 & a_n^2 & a_z^2 \\ \vdots & \vdots & \vdots \\ a_e^8 & a_n^8 & a_z^8 \end{pmatrix} \begin{pmatrix} U \\ V \\ W \end{pmatrix} \quad (3)$$

or

$$\mathbf{U}_{los} = \mathbf{A}\mathbf{U}. \quad (4)$$

The solution for  $\mathbf{U}$  is then

$$\mathbf{U} = (\mathbf{A}^T \mathbf{C}^{-1} \mathbf{A})^{-1} \mathbf{A}^T \mathbf{C}^{-1} \mathbf{U}_{los} \quad (5)$$

where  $\mathbf{C}$  is the covariance matrix of the measurements, assumed to be diagonal. These results are shown, with errors estimated from the mean square error of the inversion, in Figure 3d. The results are in good agreement with the CV estimates from panels a and b. The

background  $\mathbf{W}$  is in general within  $\pm 20$ – $50$  m/s. Errors on the resolved background winds (not including the measurement errors) are approximately 10–20 m/s.

#### 2.4. Wave Parameters Inferred From FPI Measurements

[14] The LOS winds from PKR and FYU, and the vertical winds from PKR, were band-pass filtered to identify GWs with periods of 22–42 mins. Prior to filtering, the data were interpolated to a uniform sampling rate. The sampling rate for the LOS CV measurements was  $\sim 7.5$  mins and the sampling rate for the PKZ vertical winds was  $\sim 1.2$  mins.

[15] A measured LOS wind perturbation  $\tilde{u}_i$  (for LOS  $i$ ) caused by a GW can be written as:

$$\tilde{u}_i = \tilde{u}a_e + \tilde{v}a_n + \tilde{w}a_z, \quad (6)$$

where  $(\tilde{u}, \tilde{v}, \tilde{w})$  are the components of the GW velocity vector (scaled to remove the exponential growth of the GW). If the GW wave vector does not vary in the horizontal

**Table 2.** Wave Parameters Using LOS Wind Measurements From PKR and FYU as Well as Vertical Wind Measurements From PKZ, Using Data From 2630–2800 LT<sup>a</sup>

	Value	1 $\sigma$ CI	2 $\sigma$ CI
Period, $\tau$ (min)	32.7	0.1	0.2
Background Zonal Wind, $U$ (m/s)	91.9	34.2 <sup>b</sup>	–
Background Meridional Wind, $V$ (m/s)	–127.8	25.8 <sup>b</sup>	–
Intrinsic Period, $\tau_r$ (min)	29.7	1.5	2.9
Horizontal Wavelength, $\lambda_H$ (km)	1094.1	206.4	408.6
Propagation Azimuth, $\theta$ (deg)	33.5°	8.0°	15.8°
Horizontal Wave Amplitude, $u_{H_0}$ (m/s)	28.5	4.2	8.3
Vertical Wave Amplitude, $ w'_0 $ (m/s)	18.9	0.1	0.2
Ratio of Vertical to Horizontal Amplitude, $ w'_0 /u_{H_0}$	0.66	0.15	0.29
Phase Offset between $w'$ and $u_H$ , $\psi$ (deg)	–32.4°	9.8°	19.4°

<sup>a</sup>Reduced  $\chi^2$  of fit is 0.72.

<sup>b</sup>Standard deviation.

direction, then the GW velocity components at time  $t$  at the CV location  $(x_i, y_i, z_i)$  can be written, for example, as:

$$\tilde{u} = \tilde{u}_0 \exp[i(kx_i + \ell y_i + mz_i - \omega_r t)]. \quad (7)$$

Then, equation (6) becomes

$$\tilde{u}_i = [\tilde{u}_0 a_e + \tilde{v}_0 a_n + \tilde{w}_0 a_z] e^{i(kx_i + \ell y_i + mz_i - \omega_r t)}. \quad (8)$$

For measurements relative to  $(x_0, y_0, z_0, t_0)$ , and assuming that all measurements are made at the same altitude (i.e.,  $z_i = z_0$ ), we can write the GW LOS perturbation, from equation (8), as

$$\tilde{u}_i(t) = [\tilde{u}'_0 a_e + \tilde{v}_0 a_n + \tilde{w}_0 a_z] e^{i\alpha_i} \quad (9)$$

where the phase is  $\alpha_i = k(x_i - x_0) + \ell(y_i - y_0) - \omega_r(t - t_0) + \beta$ , and  $\beta$  is a constant phase offset at  $(x_0, y_0, z_0, t_0)$ .

[16] Following equation 20 from VN2012 relating the zonal and meridional wind components to the horizontal wind component, we write the GW velocity amplitudes as

$$\tilde{u}_0 = \frac{k}{k_H} \tilde{u}_{H0}, \tilde{v}_0 = \frac{\ell}{k_H} \tilde{u}_{H0}, \tilde{w}_0 = b e^{i\psi} \tilde{u}_{H0} \quad (10)$$

where  $\tilde{u}_{H0}$  is the GW horizontal velocity amplitude,  $b\tilde{u}_{H0}$  is the GW vertical velocity amplitude ( $b$  is a scaling factor), and  $\psi$  is the phase difference between the GW vertical and horizontal velocity components. Then, equation (9) becomes

$$u'_i(t) = \left[ \frac{k}{k_H} a_e + \frac{\ell}{k_H} a_n + b e^{i\psi} a_z \right] u_{H0} e^{i\alpha_i}. \quad (11)$$

Using measurements of  $\tilde{u}_i$  as a function of time at multiple locations, we can then fit for the unknown parameters:  $\omega_r$ ,  $k$ ,  $\ell$ ,  $\psi$ ,  $u_{H0}$ ,  $b$ , and  $\beta$ .

[17] Using the data from 2630–2800 LT, the LOS data from PKR and FYU as well as the vertical wind data from PKZ were fit using this procedure. To account for the smearing of the gravity wave perturbations horizontally and vertically over the emission layer, the emission layer was assumed to be centered at 260 km with a half-width of 100 km. The forward model then included a spatially weighted average over the

emission layer and a smoothing in time given by the integration time of the measurements (7.5 mins for the PKR and FYU measurements). In order to identify a global minimum solution, a fitting procedure was performed wherein the initial guess for the unknown horizontal wavelength and the propagation azimuth were varied systematically. For each fit, the initial value of the phase angles ( $\psi$  and  $\beta$ ) were chosen randomly, and this was repeated  $\sim 100$  times with different initial conditions. The best solution was chosen as that with the lowest squared 2-norm of the residual.

[18] The results of the fitting procedure are shown in Figure 4. Figure 4 (top) shows the fitted wave at the location of Poker Flat. The vertical velocity leads the horizontal velocity, and the fitted and measured vertical velocities are very similar before 28 LT. The wave could be propagating either northeast (NE)ward or southwest (SW)ward, as suggested by  $u'$  and  $v'$  being in phase. Because  $v' > u'$ , the GW is propagating more meridionally than zonally. Figure 4 (bottom) shows the fitted and measured LOS velocities at the locations of the 4 CVs. In general, the results agree reasonably well; however, the LOS velocity measured at CV1 is much larger than the fitted value at 2645–2745 LT. Therefore, while the fit is good for these data, there are significant differences between the measured and fitted values, leading to a possible misestimation of  $u_{H0}'$ . In addition, the results of the fit are sensitive to the chosen time window for the analysis.

[19] Table 2 shows the forward model results and average background wind. Because the results are sensitive to the chosen time window, we utilize the 2 $\sigma$  confidence intervals as most representative of the errors of these results. We find this GW to be medium to large scale, with a horizontal wavelength  $\lambda_H = 1094 \pm 409$  km (i.e.  $\lambda_H \sim 685$ –1503 km), a ground-based period  $\tau_r = 32.7 \pm 0.2$  min, and a corresponding ground-based phase speed  $c_H \sim 350$ –770 m/s. The wave was determined to be propagating NEward at an azimuth angle (clockwise from north)  $\theta = 33.5 \pm 15.8^\circ$ . A solution for a GW propagating SWward was also found; however, this solution was unphysical (see below), and so was discarded. The GW vertical velocity leads the horizontal velocity in time by  $32.4 \pm 19.4^\circ$ . Because this difference is statistically different from zero, it implies a GW vertical wavelength of  $| \lambda_z | \sim (2-4)\pi\mathcal{H}$  such that compressible effects are somewhat important (VN2012).

[20] Note that there were other solutions with similar (but not quite as low) squared 2-norm of the residuals. In particular, a reasonably good solution was found for a SWward-propagating wave with a short horizontal wavelength ( $\lambda_H < 100$  km). However, this solution is confirmed as unlikely given that such a wave would be propagating with the wind, leading to a negative intrinsic frequency, which is an unphysical solution. Thus, we believe the solution that the fitting technique converged on is the most likely, both on statistical and physical grounds.

[21] We used a slightly different procedure to fit the PKZ temperature and vertical velocity data to determine the phase relationship between those parameters. The data from the PKZ instrument were unequally-spaced and had small data gaps. First, we subtract the mean for  $w'$  and  $T'$ , then we fit using the unfiltered data. These results are shown in Figure 5 and Table 3. We see that the fitted results agree reasonably well with the data before 2745 LT. The phase difference between  $T'$  and  $w'$  is  $-81.4 \pm 56.5^\circ$ , and the average

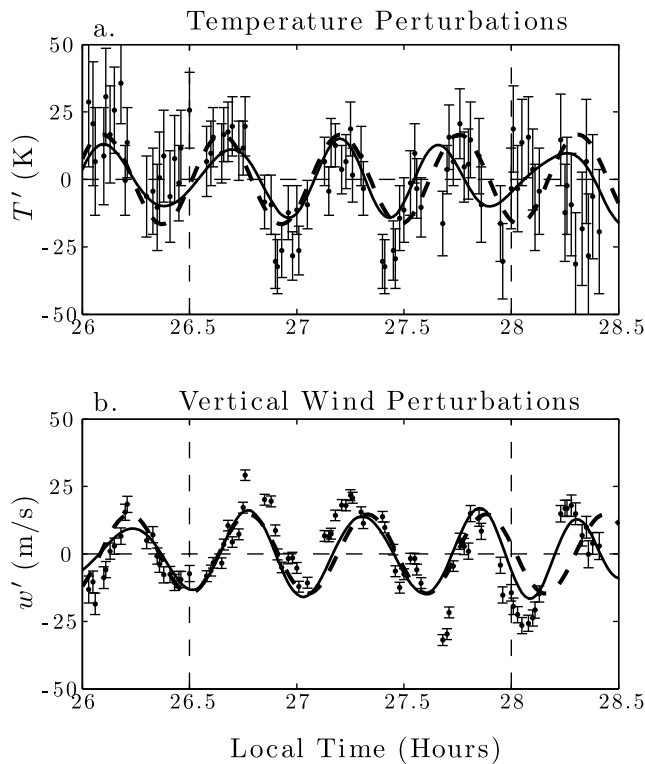


**Figure 5.** (a) Temperature with mean subtracted (points with error bars), filtered temperature perturbations (solid line), and forward model fit (dashed line). (b) Same for vertical wind.

background temperature is  $\bar{T} = 640$  K. We will compare these results with GW dissipative theory in section 3.

### 2.5. Poker Flat SDI Observations

[22] It is desirable to confirm the direction of propagation extracted from the previous analysis. This is especially true since the extracted horizontal wavelength was large and error-prone, a result of the small and difficult-to-measure phase delay between different LOS measurements. The Poker Flat SDI, an all-sky imaging Fabry-Perot spectrometer [Conde and Smith, 1995, 1997, 1998], was also operating on this night. This system and its operation has been most recently described in Conde and Nicolls [2010]. The SDI divides its  $75^\circ$  field-of-view (FOV) into 115 observing zones, within each of which the LOS neutral wind can be determined. The tradeoff with the all-sky measurements (that allows, for example, for spatially resolved wind measurements) is a larger FOV of each LOS measurement as compared to the FPI measurements previously described, as well as reduced sensitivity in any single zone.

[23] Zones were selected where wave perturbations were clearly observed and zenith angles were sufficiently small (such that the FOV of the zones was not too large). These zones and corresponding LOS wind perturbations are shown in Figure 6 as a function of zonal and meridional distance from Poker Flat. The selected zones were in the region overhead and northward of Poker Flat, where signal intensities were highest, and hence errors were lowest. The approximate FOV of each zone at 300 km is plotted; for the overhead zone, the FOV extends  $\sim 24^\circ$ , with a radius of

**Table 3.** PKZ Wave Parameters, Using Data From 2630–2800 LT<sup>a</sup>

	Value	$1\sigma$ CI	$2\sigma$ CI
Period, $\tau$ (min)	33.2	0.6	1.2
Temperature Amplitude, $T_0'$ (K)	16.6	6.1	12.2
Vertical Wave Amplitude, $w_0'$ (m/s)	14.7	1.6	3.2
Phase Offset between $T'$ and $w'$ (deg)	$-81.4^\circ$	$28.5^\circ$	$56.5^\circ$
$100(T_0'/T)/w_0'$	0.18	0.07	0.14

<sup>a</sup>Reduced  $\chi^2$  of fit is 11.3.

$\sim 60$  km at 300-km altitude. Altitude variation of the emission layer extends the FOV of each zone. Linearly detrended LOS winds are plotted as black curves, and band-pass filtered LOS winds (similar to the previous section) are plotted as red curves, for the time period 2630–2800 LT.

[24] In Figure 7, we plot the wind perturbations from selected zones as a function of time and horizontal distance from the first zone. The zones plotted in each column have been selected to lie on an approximately horizontal line, the azimuth of which is shown above each plot. The first column corresponds to a  $\sim$ northeastward line, the second to a  $\sim$ northward line, the third to an  $\sim$ eastward line, and the fourth to a  $\sim$ northwestward line. The perturbations show a wave with a period of  $\sim 35$  mins, roughly consistent with the results from the previous section. The first two columns show consistency with a  $\sim$ northward propagating wave: the perturbations (ignoring the possibility of spatial aliasing) are seen first in the most southward zones. The third column shows perturbations that are roughly in phase, also consistent with a predominantly northward-propagating wave.

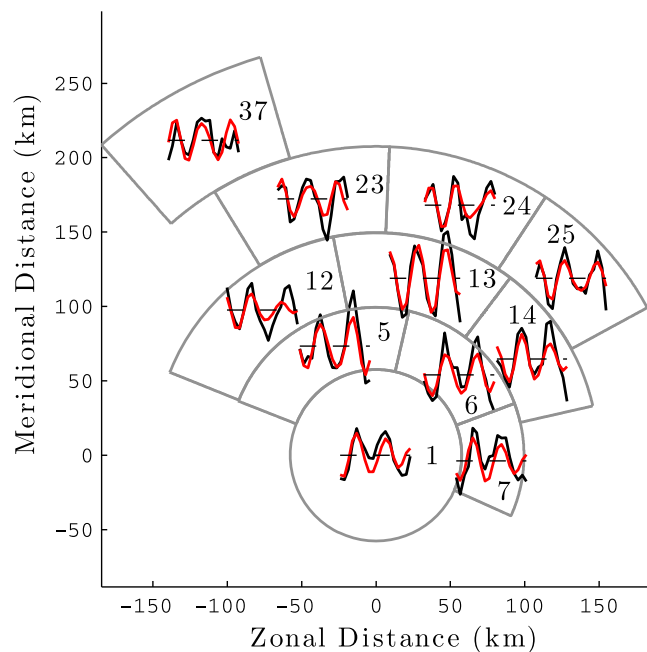


**Figure 6.** Poker Flat SDI observations of line-of-sight winds from selected zones for the period 2630–2800 LT (1130–1300 UT). Black lines correspond to linearly detrended LOS winds, and red lines correspond to filtered winds. Zones are numbered and the approximate field-of-view of each zone at 300 km altitude is plotted.

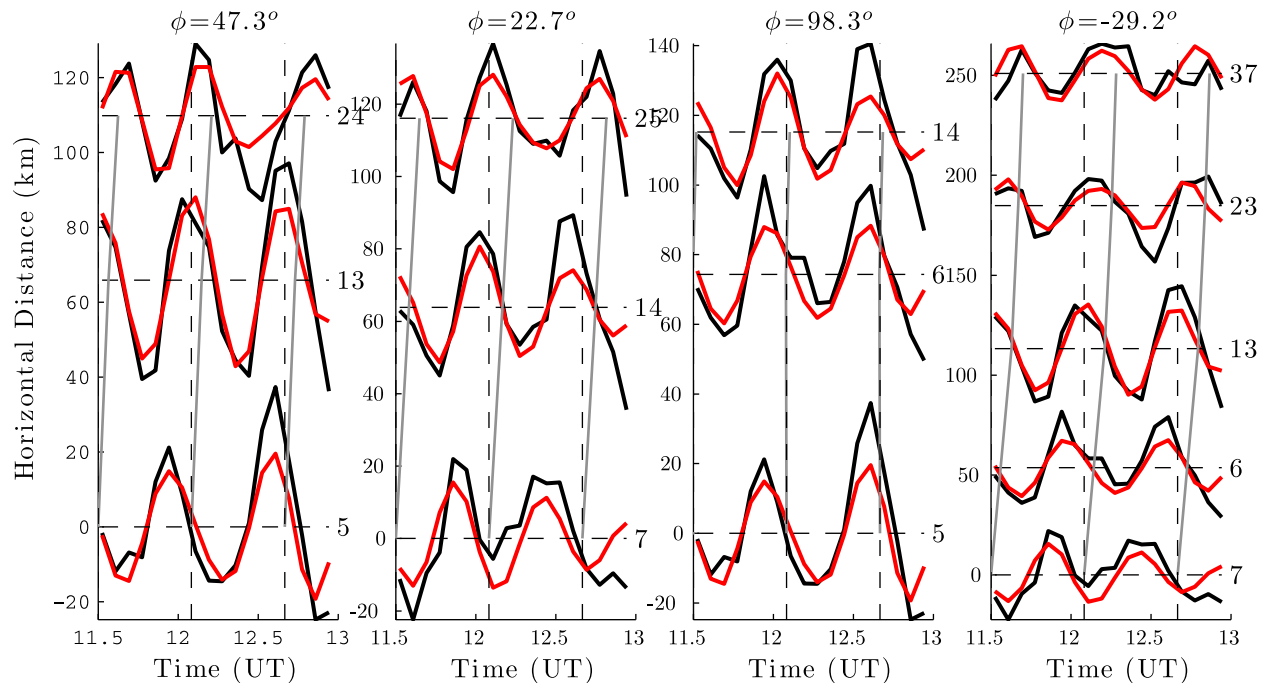


**Figure 7.** LOS wind perturbations for selected zones from Figure 6. The average azimuth of the horizontal line connecting the measurements is indicated in the title, and the zone number is indicated to the right of each dashed line. Black lines correspond to linearly detrended LOS winds, and red lines correspond to filtered winds. The gray diagonal line connecting the zones is the estimated line-of-constant-phase as described in the text.

[25] A cross-correlation analysis was performed to identify the dominant phase offset between all zones. The best fit from this cross-correlation analysis are shown as the gray lines-of-constant-phase in Figure 7. These phase offsets (assuming no aliasing) were resolved into a horizontal wavelength and propagation azimuth. The results of this analysis were  $\lambda_H = 442 \pm 166$  km and  $\theta = 10.9 \pm 19^\circ$ . The results were sensitive to the chosen zones, but azimuths ranged from  $\sim -10^\circ$  to  $60^\circ$ , and horizontal wavelengths from 200–300 km up to about 1000 km.

[26] These results are broadly similar to and confirm those of the previous section, with the exception of the deduced horizontal wavelength of the wave, which is quite a bit smaller. Given the large errors on the deduced horizontal wavelength in the previous section, and the fact that the measurements are not exactly co-located, we do not place much emphasis on this discrepancy. For the remainder of this paper, we will use the results of section 2.4.

## 2.6. PFISR Observations

[27] PFISR, co-located with the PKZ instrument, can also observe GWs. In contrast to daytime measurements [Nicolls and Heinselman, 2007; Vadas and Nicolls, 2008], reasonable nighttime, winter measurements are typically only available during auroral conditions. Although PFISR can in principle detect GWs during these conditions, the rapid variability induced by auroral precipitation and convection can make detection and identification difficult.

[28] On 10 January 2010, from 07–13 UT (i.e., 22–26 LT on 9–10 January), PFISR operated in a mode with 5 beams clustered around the local magnetic zenith. None of the

beams looked directly vertically. The signal-to-noise ratio from the long pulse showed a period of very weak precipitation prior to  $\sim 1145$  UT followed by a period of enhanced precipitation, as shown by the raw electron density  $N_e$  in Figure 8 (top left). Most of the variability in  $N_e$  was due to auroral processes, and without the knowledge of a wave present from the Fabry-Perot data, we would not attempt to identify any gravity wave effects from the PFISR measurements. Figure 8 (top right) shows the filtered electron density perturbations,  $\delta N_e / \bar{N}_e$ . Fluctuations with a period of  $\sim 30$  min are visible. Because of the small beam spacing,  $\lambda_H$  and  $\theta$  could not be determined for this wave as has been done previously [Nicolls and Heinselman, 2007].

[29] Figure 8 (bottom left) shows the LOS ion speeds ( $V_{los}$ ). The data contains dominant high-frequency components. The lower right panel shows  $V_{los}$  smoothed over 13 min, as well as band-pass filtered. Perturbations with a period around  $\sim 30$  min are visible in a spectral analysis (not shown) and in the smoothed results. The amplitude of the perturbations seems to increase with altitude, the expected behavior for a traveling ionospheric disturbance (TID) induced by a non-dissipating GW. At the two middle altitudes, the wave phase progresses downward in time, indicating an upward-propagating GW. At  $z = 310$  km, the wave has a somewhat smaller period, which might be due to auroral or other plasma effects.

[30] In order to estimate the vertical wavelength,  $\lambda_z$ , of this wave, we cross-correlate the filtered signals at 240 and 275 km altitude and find a peak within the approximate range of delays  $\sim 1.73$ – $3.3$  min. PFISR's beam was pointed

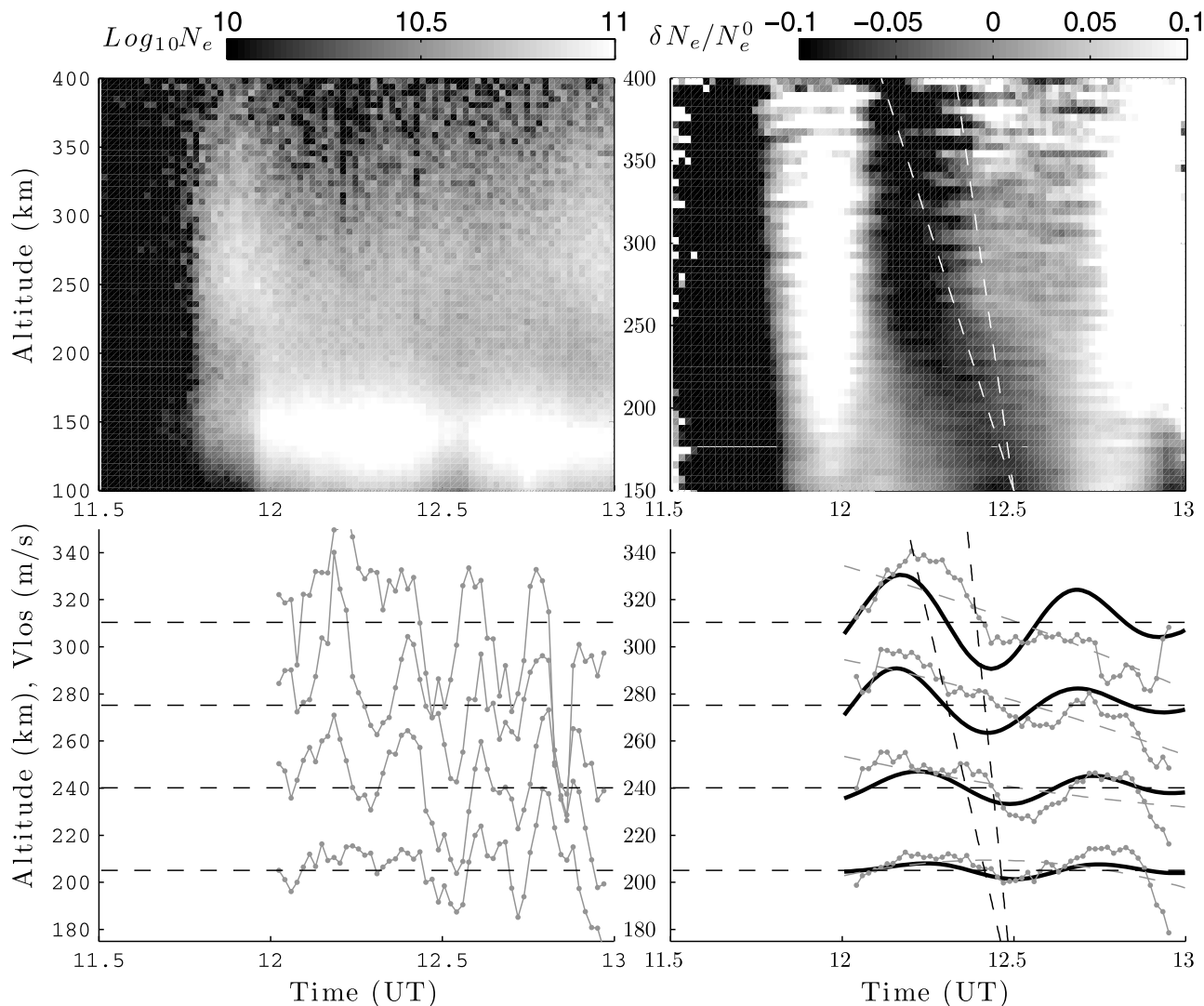


**Figure 8.** (top left) Raw electron density,  $N_e$ , 1 minute data, measured by PFISR. (top right)  $\delta N_e / \bar{N}_e$ .  $\bar{N}_e$  was determined by applying a 50 min low-pass filter.  $\delta N_e$  was determined by using a 20 min running average and subtracting  $\bar{N}_e$ . The thin dashed line shows  $\hat{v}$  from the bottom right panel. (bottom left)  $V_{los}$  in m/s (with mean subtracted) after smoothing with a 3 point (3 min) running average (thin gray lines with dots). These values are shown at the 4 altitudes of 205, 240, 275, and 310 km, as shown by the dashed horizontal lines. (bottom right) 13-minute smoothed  $V_{los}$  (gray dots) along with a polynomial fit (gray dashed line). Dark black lines show the result of band-pass filtering  $V_{los}$  (from 25 to 40 min). The thin dashed line shows the range of extracted vertical phase velocities,  $V_{ph} \approx -180$  to  $-410$  m/s.

at an azimuth of  $-153^\circ$  (SWward). We estimate  $\lambda_z$  by inputting the GW parameters  $\lambda_H$  and  $\theta$  (see Table 2) into equation 29 of *Vadas and Nicolls* [2009]. Including the errors from the GW parameters, these results lead to vertical wavelength estimates within the range of  $\sim -350$  to  $-800$  km. Note that errors caused by propagation of the  $2\sigma$  errors on the fitted parameters (from Table 2) are much smaller ( $\sim 10$ – $50$  km) than the errors in determining the vertical phase velocity of the wave,  $|V_{ph}|$ .

[31] These values of  $\lambda_z$  correspond to a vertical phase velocity  $V_{ph} \approx -180$  to  $-410$   $\text{ms}^{-1}$ , a range which is represented by the thin, nearly vertical dashed lines in Figure 8 (bottom right). We overplot these dashed lines in the upper right panel, and see that the  $dN_e / \bar{N}_e$  phase lines agree

reasonably well with these results, indicating that this wave seems to be visible in both the  $N_e$  and  $V_{los}$  measurements. However, it is unclear how much of the density perturbations is caused by auroral ionization enhancements and transport.

[32] Plasma oscillations are induced by a GW via neutral-ion collisions. The  $V_{los}$  perturbations looking up the magnetic field line should be approximately equal to the GW's vertical velocity,  $w'$ , since the magnetic field is nearly vertical at Poker Flat, with a dip angle  $\sim 77.5^\circ$  [*Nicolls and Heinselman*, 2007]. Figure 9 (top) shows a comparison of  $w'$  measured by PKZ and  $V_{los}$  measured by PFISR, and the band-pass filtered signals. Although the PFISR data are noisy, we see that  $w'$  and  $V_{los}$  have approximately equal amplitudes, the expected result if the neutral GW pushes the

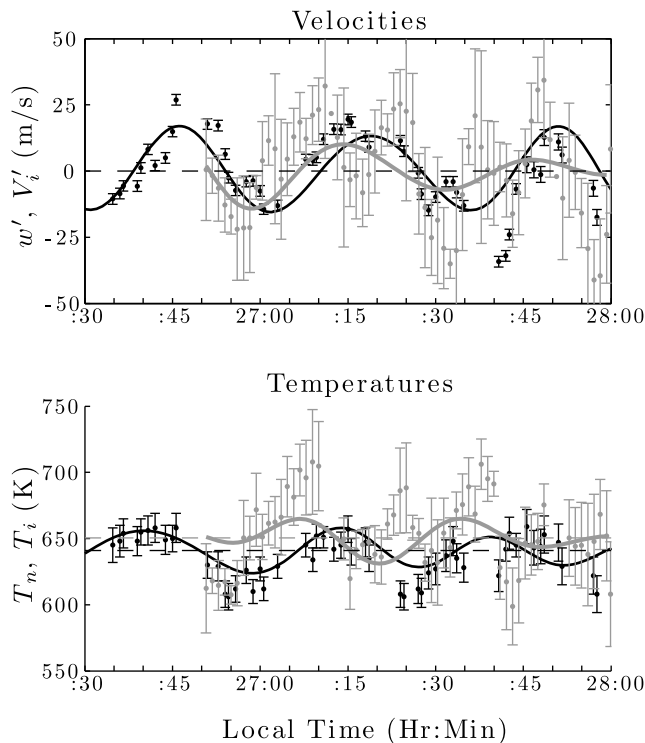


**Figure 9.** Comparison of FPI (black) and PFISR (grey) data and band-pass filtered signals (lines). (top)  $w'$  measured by PKZ and the ion velocity along the field-line ( $V_{los}$ ) measured by PFISR. (bottom)  $T$  measured by PKZ and  $T_i$  measured by PFISR. Dashed lines show the median values over this time window, which are within 10 K (well within the error bars of the measurements).

ions via ion drag at this location. Additionally, the PFISR signal leads the PKZ signal by  $\sim 6$  minutes. This is consistent with a northward propagating wave, because PKZ is observing directly above Poker, while the PFISR beam intersects the thermosphere south of Poker Flat.

[33] *Conde and Nicolls* [2010] compared the ion temperature,  $T_i$ , from PFISR and the neutral temperature,  $T$ , from the Poker Flat SDI, and found that they agree reasonably well, even over short time periods, for long-term (several-month) data sets. Figure 9 (bottom) shows  $T$  measured by PKZ and  $T_i$  measured by PFISR, and the band-pass filtered signals. The absolute temperature values agree well, in agreement with *Conde and Nicolls* [2010]. Additionally, the perturbation amplitudes are quite similar. As expected, the PFISR signal leads the FPI signal.

### 3. Comparison of GW Dissipative Theory With Measurements

[34] We now compare the extracted GW parameters with the GW dissipative dispersion and polarization relations derived in the companion paper (VN2012). The GW parameters, phase shifts, and component amplitudes determined by the FPI forward model results and PFISR observations are quite extensive, and contain crucial information on the GW temperature and amplitude perturbations that allow us to make a direct comparison with theory. Each determined

result, such as  $\omega_r$ ,  $|w'_0/u'_{H0}|$ , or the phase shift between  $w'$  and  $u'_H$ , restricts the range of  $\lambda_H$ ,  $\lambda_z$ , and  $\theta$  allowed by this dissipative theory. It is important to compare these results and observations with the GW theory presented in VN2012 to see if there is a region of overlap between these restricted ranges of allowed GW parameters. Such an overlap in GW parameter space is essential for validating the GW theory and its inherent assumptions.

[35] The altitude range for the 630-nm emission is 200–300 km. For the purpose of obtaining a realistic range of background parameters from the idealized and MSIS profiles, we search in parameter space from 200–300 km altitude. Using the average observed neutral temperature of  $\bar{T} = 640$  K, we estimate kinematic viscosities,  $\nu$ , in the range  $10^5$  to  $10^7$  m<sup>2</sup>/s (see Figure 6a of VN2012). Using this range of  $\nu$ , we estimate  $\mathcal{H} = 20$ –40 km,  $N_B = 0.009$ –0.011 rad/s and  $c_s = 580$ –750 m/s (see Figures 6b–6d of VN2012). Using the PFISR data from section 4.5, we estimate  $|\lambda_z| \approx 300$ –800 km. This range for  $\lambda_z$  overlaps with  $|\lambda_z| \sim (2$ – $4)\pi\mathcal{H} \sim 125$ –430 km from section 2.4. From the FPI results in Table 2,  $\lambda_H$  is in the range  $\sim 685$ –1500 km, and  $w'$  leads  $u'_H$  in time by 13 to 52°. Leading in time equates to a positive  $w' - u'_H$  phase shift in  $x$ . From VN2012, the phase shift for a large- $|\lambda_z|$  GW is typically negative (i.e.,  $u'_H$  leads  $w'$ ), not positive, except for certain values of  $\lambda_H$  when  $\nu$  is quite large (i.e.,  $\nu \geq 10^5$  m<sup>2</sup>/s). Additionally, the fitted ratio of the vertical to horizontal velocity amplitudes is quite sensitive to  $\bar{T}$  and  $N_B$ .

[36] We perform a search in parameter space using the GW dissipative dispersion and polarization relations to determine which upward-propagating GWs fit the FPI and PFISR results. We allow  $\lambda_H$  and  $\theta$  to range over their values in Table 2 with  $2\sigma$  errors, and allow  $\lambda_z = -800$  to  $-300$  km, as discussed above. These values are varied independently of each other. We constrain  $\tau_r$ ,  $\tau_{Ir}$ , and the  $w' - u'_H$  and  $T' - w'$  phase shifts to their values in Tables 2 and 3 with  $2\sigma$  errors. We allow  $w'_0/u'_{H0}$  to be somewhat lower than the  $2\sigma$  result in Table 2:  $0.25 < w'_0/u'_{H0} < 0.95$ . We also allow  $100 T'_0/\bar{T}/w'_0$  to be somewhat larger than the  $2\sigma$  result in Table 3:  $0.04 < 100 T'_0/\bar{T}/w'_0 \leq 0.6$ .

[37] We now determine reasonable ranges over which to vary the background parameters. Figure 10 shows the temperature profile on this evening at 12 UT from the empirical NRLMSISE-00 model [*Picone et al.*, 2002]. The exospheric temperature is  $\bar{T} = 614$  K, which underestimates the measured

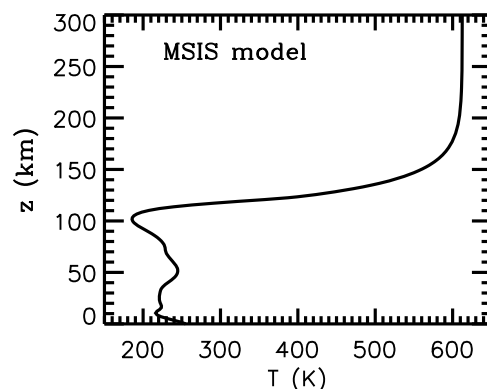


**Figure 10.** MSIS background temperature,  $\bar{T}$ , at 12 UT.

value by  $\sim 25$  K. From  $z = 200$  to  $300$  km, the parameter ranges from MSIS are  $\mathcal{H} = 25\text{--}35$  km,  $c_s = 630\text{--}770$  m/s,  $\gamma = 1.55\text{--}1.67$ ,  $\nu = 10^5\text{--}6 \times 10^6$  m<sup>2</sup>/s, and  $N_B = 0.009\text{--}0.011$  rad/s. This range of  $N_B$  corresponds to buoyancy periods of  $\tau_B = 2\pi/N_B = 9.5\text{--}12$  min, with the larger value being at the highest altitude. However, because  $\tau_B$  increases substantially as  $\bar{T}$  increases [e.g., *Yeh and Liu, 1974; Yiğit and Medvedev, 2010*], and because  $N_B$  is the vertical derivative of the potential temperature, which can depart from the MSIS profile because of tides and auroral effects, we extend our search to range over  $N_B = 0.007\text{--}0.011$  rad/s, where the lower limit corresponds to  $\tau_B = 15$  min. We allow the background wind components,  $U$  and  $V$ , to range over their values in Table 2. Using both the MSIS and idealized values shown in Figure 6 of VN2012 for  $\bar{T} \sim 700$  K, we allow the background values to be  $\mathcal{H} = 20\text{--}40$  km,  $c_s = 580\text{--}770$  m/s,  $\gamma = 1.55\text{--}1.67$ ,  $\nu = 10^5\text{--}10^7$  m<sup>2</sup>/s, and  $N_B = 0.007\text{--}0.011$  rad/s. All of these background values are varied independently of each other.

[38] Figure 11 shows the results of this search. Several hundred thousand GWs are found within this allowed range of GW and background parameters. (This number depends on how finely we subdivide the variables that vary in our search.) These GWs have  $\lambda_H \sim 700\text{--}1100$  km,  $|\lambda_z| \sim 350\text{--}500$  km,  $\tau_{H'} \sim 26\text{--}32$  min, and are propagating NEward with  $\theta \sim 15\text{--}50^\circ$ . These GWs have ground-based phase speeds of  $c_H = \omega_r/k_H \sim 350\text{--}560$  m/s. Additionally,  $w'$  leads  $u'_H$  by  $10\text{--}20^\circ$ ,  $T'$  leads  $w'$  by  $30\text{--}50^\circ$ , and  $w'_0/u'_{H0} = 0.25\text{--}0.3$ . (The fitted value with  $2\sigma$  errors is  $w'_0/u'_{H0} = 0.37\text{--}0.95$ .) The temperature amplitude ratio is somewhat too large; the fitted ratio of the temperature to vertical velocity with  $2\sigma$  errors is  $100(T'_0/\bar{T})/w'_0 = (0.18 \pm 0.14)$  (m/s)<sup>-1</sup>, the GW solutions yield somewhat larger values of  $100(T'_0/\bar{T})/w'_0 \geq 0.47$  (m/s)<sup>-1</sup>. However, both of these ratios depend sensitively on  $N_B$  and  $H$ , which involve (unmeasured) derivatives of  $\bar{T}$  and  $\bar{\rho}$ . For example, larger buoyancy periods tend to increase  $w'_0/u'_{H0}$  and decrease  $100(T'_0/\bar{T})/w'_0$ . Figure 11i shows the dissipation factor,  $\epsilon$ , from equation 24 of VN2012. All of these GWs have  $\epsilon \geq 1$ , and most have  $2 \leq \epsilon \leq 5$ ; therefore, most of these GWs are not yet strongly dissipating.

[39] While there is only a weak dependence of the solutions shown in Figure 11 on  $c_s$ ,  $\bar{U}$ , and  $\bar{V}$ , the solutions are peaked strongly at  $\nu = 3 \times 10^6$  m<sup>2</sup>/s,  $\mathcal{H} = 40$  km, and  $\tau_B \sim 13\text{--}15$  min. For the MSIS and idealized temperature profiles discussed previously, these values imply altitudes of  $z = 270\text{--}300$  km. This is the upper portion of the 630-nm emission layer, and suggests that the largest contribution to this emission from the GW occurs at the highest altitudes in this layer. Because a non-dissipating GW's amplitude grows exponentially with altitude, and because  $\epsilon \geq 1$  from Figure 11i, this suggests that the observed GW's amplitude is increasing over this layer. Figure 8 (bottom right) supports this conclusion, since the amplitude of  $V_{los}$  grows rapidly with altitude from  $z = 205$  to  $275$  km, and is somewhat larger at  $310$  km than at  $275$  km.

[40] We now restrict our results to only those GWs at the peak of the distribution with  $\lambda_H = 875$  km and  $\lambda_z = -400$  km. Approximately 9000 GWs are identified. These GWs have  $\tau_{H'} = 27\text{--}29$  min,  $\theta = 17\text{--}48^\circ$ ,  $\epsilon = 2.0\text{--}2.5$ ,

$c_H = 445$  m/s,  $c_s = 580\text{--}770$  m/s,  $\mathcal{H} = 40$  km,  $\gamma = 1.61\text{--}1.67$ , and  $\tau_B = 14\text{--}15$  min. Figure 12 shows a typical solution for  $\theta = 30^\circ$  and  $\tau_{H'} = 28$  min. For this solution,  $\bar{U} = 116$  m/s and  $\bar{V} = -154$  m/s. This GW's ground-based phase speed is  $c_H = \omega_r/k_H = 445$  m/s, which is much larger than the speed of sound in the lower atmosphere. Therefore, this GW cannot propagate (or be excited) in the lower atmosphere (i.e., the troposphere, stratosphere, or mesosphere). Here, we have chosen a wave amplitude of  $u'_{H0} = 28.5$  m/s from Table 2, and include an arbitrary phase offset in time for  $u'_H$ . We then calculate  $u'$ ,  $v'$ ,  $w'$ , and  $T'$  from  $u'_H$  using the compressible, dissipative polarization relations (equations 15–17 and 20 of VN2012). Figure 12a shows this theoretical GW's zonal, meridional, and vertical velocity perturbations at the location of Poker Flat. Figure 12b shows its vertical velocity and temperature perturbations (using  $\bar{T} = 640$  K). Overall, the agreement with the FPI forward model results (Figure 4, top) is quite good. This GW displays the most important properties of the observed GW; this theoretical GW has  $\lambda_H$  within the range of expected values, is traveling NEward in the observed direction, has the correct observed and intrinsic periods, has a larger meridional than zonal velocity, has a vertical velocity which leads the zonal and meridional velocities in the fitted range, and has a temperature perturbation which leads the vertical velocity in the fitted range. Additionally, the amplitude of  $T'$  is within  $2\sigma$  errors from Table 3. The only discrepancy is that the fitted amplitude of  $w'$  is somewhat too small. This is likely partly due to the sensitivity of the solutions to  $N_B$  and  $\mathcal{H}$ , which are unmeasured. It may be due to partial interference with a smaller-amplitude GW, or to error in the FPI measurements or analysis. Finally, it may also be due to the fact that  $|\lambda_z|$  may be only slightly smaller than  $4\pi\mathcal{H}$ , which is the limit of the assumption for the theory derived in this paper.

#### 4. Possible GW Sources

[41] From the FPI measurements, the observed GW had a ground-based phase speed of  $c_H = 350\text{--}770$  m/s. The GW's intrinsic phase speed was likely greater than  $\sim 310$  m/s, and thus it probably originated in the thermosphere. If its intrinsic phase speed were less than  $\sim 310$  m/s (possible given the measurement uncertainties, but not likely), it may have originated from a source in the lower atmosphere.

[42] Possible lower-atmospheric sources of this GW ( $c_{IH} < 310$  m/s) include (N.B., because this is a wintertime observation, deep convection cannot be considered as a likely source of this GW):

[43] 1. Secondary GWs from mountain-wave breaking in the stratosphere or mesosphere, or possibly direct mountain waves from gusty wind flow. Figure 13 shows vectors of the winds at  $\sim 5$  km ( $\sim 16400$  ft). The winds are mostly south-eastward with a magnitude of  $16\text{--}20$  m/s over the mountains  $400$  km south of Poker Flat. We estimate a nondimensional mountain height of  $hN_B/U \sim 4\text{--}5$ , a value that can be associated with significant mountain-wave generation. Mountain waves were therefore likely excited that evening. If the wind was quite gusty, mountain waves with non-zero phase speeds could have been excited; if energetic enough, some of these GWs might have propagated directly to the thermosphere. More likely, the mountain

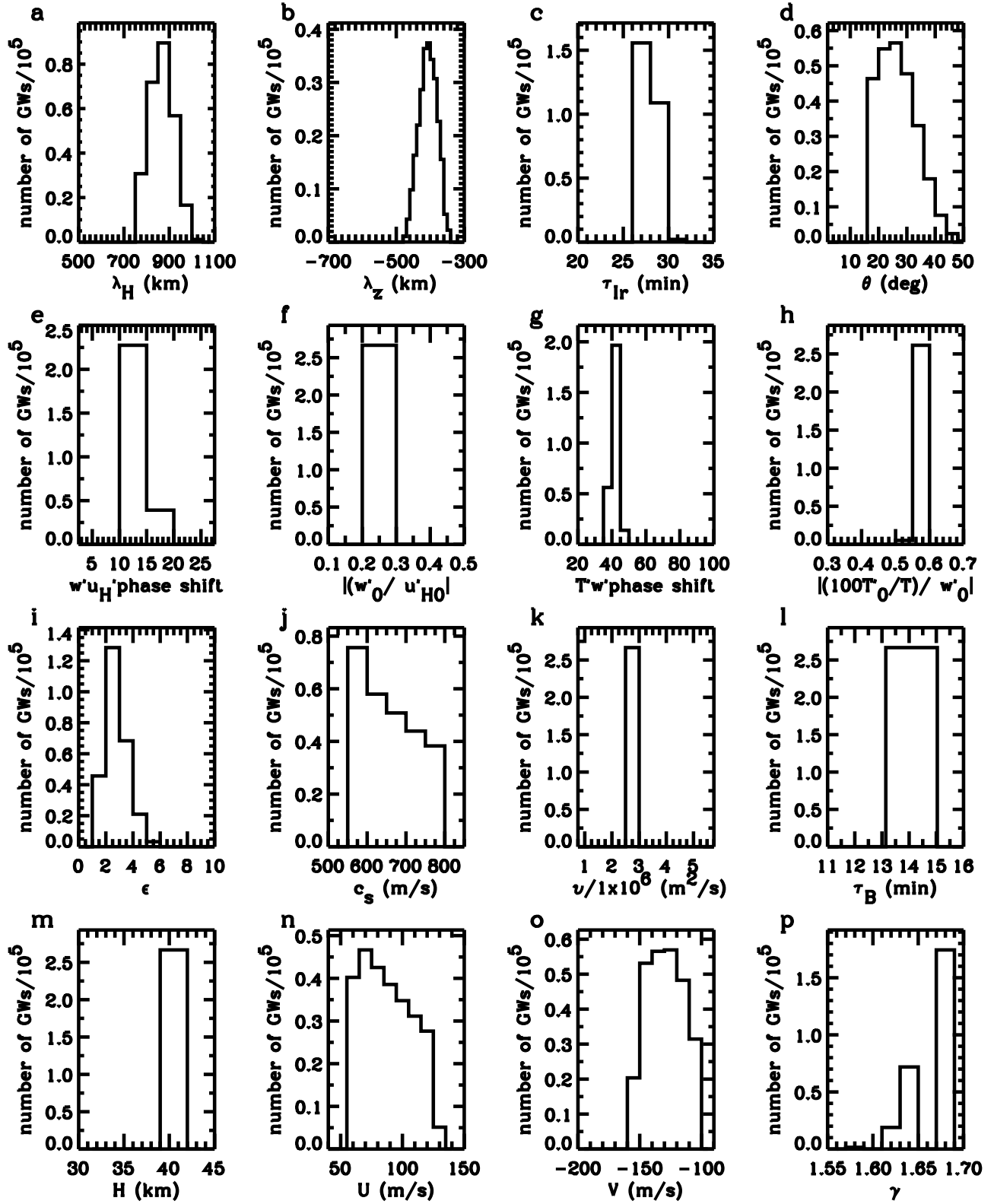
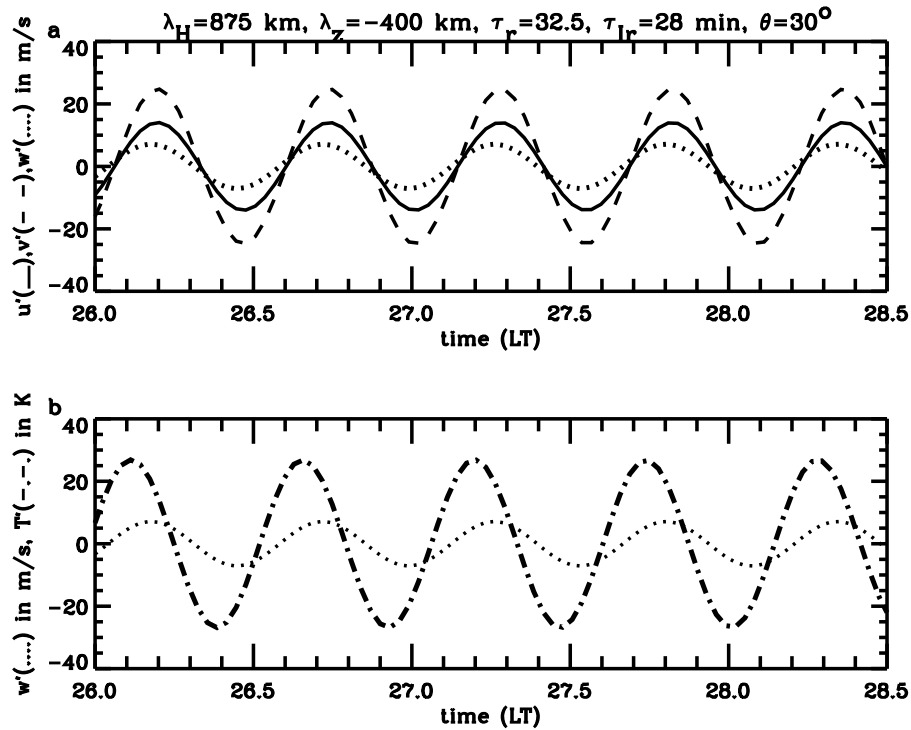


Figure 11. Parameters of the GWs and background fluid which lie within the range of fitted GW values and background values, as described in the text. (a)  $\lambda_H$ . (b)  $\lambda_z$ . (c)  $\tau_{lr}$ . (d)  $\theta$ . (e)  $w' - u'_H$  phase shift. (f)  $w'_0/u'_{H0}$ . (g)  $T' - w'$  phase shift. (h)  $(100 T'_0/T)/w'_0$ , (i)  $\epsilon$ . (j)  $c_s$ . (k)  $\nu/1 \times 10^6$ . (l)  $\tau_B = 2\pi/N_B$ . (m)  $H$ . (n)  $U$ . (o)  $V$ . (p)  $\gamma$ .



**Figure 12.** One of the theoretical GW solutions from Figure 11 at the peak of the distribution using  $\max(u_H) = 24.6$  m/s. This GW has  $\lambda_H = 750$  km,  $\lambda_z = -450$  km,  $\theta = 20^\circ$ ,  $\tau_{IR} = 26$  min, and  $\tau_r = 32$  min. The values are calculated at PF at  $z = 260$  km. An arbitrary time offset has been added. (a)  $u'$  (solid),  $v'$  (dashed), and  $w'$  (dotted). (b)  $w'$  (dotted) and  $T'$  (dash-dotted).

waves would have broken in the stratosphere or mesosphere [Fritts and Alexander, 2003], exciting larger-scale secondary GWs with larger phase speeds, which could have then propagated to  $z \sim 250$  km.

[44] 2. GWs excited by cold fronts or frontal systems [Laštovička, 2006].

[45] More likely, this GW originated in the thermosphere. Possible thermospheric sources of this GW include ( $c_{IH} > 100$  m/s):

[46] 3. Shear-generated GWs [Fritts and Alexander, 2003]. Here, the neutral wind shear may have been created by auroral convection.

[47] 4. Tertiary GWs excited by the dissipation of secondary GWs from mountain-wave breaking in the stratosphere or mesosphere. In this scenario, the secondary GWs excited by the breaking of mountain wave waves south of PFISR (as discussed above) would propagate into the thermosphere and dissipate below  $z < 200$ – $225$  km. (Note that GWs observed by PFISR during the daytime winter over Alaska in 2006 were identified as likely being secondary GWs from mountain wave breaking [Vadas and Nicolls, 2009]). The dissipation of these secondary GWs accelerates the neutral fluid, and excites larger- $\lambda_H$  and larger- $c_H$  tertiary GWs [Vadas and Liu, 2009]. Those larger- $\lambda_H$  tertiary GWs propagating northward could be detected by PFISR and the FPI network.

[48] 5. GWs excited by auroral forcing [e.g., Hocke and Schlegel, 1996; Walterscheid et al., 1985; Mayr et al., 1987], perhaps via Joule heating, direct particle precipitation, Lorentz forcing, or induced horizontal body forces associated with auroral convection / ion drag. In this latter

mechanism, the horizontal body forces are in response to the rapid changes in the neutral background wind from auroral convection and ion drag; GWs are then excited in response to these temporally evolving body forces [Vadas and Fritts, 2001]. The observed GW horizontal wavelength and period

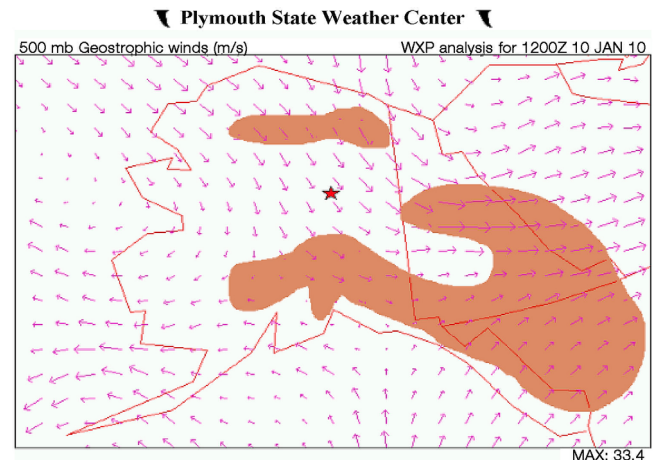


**Figure 13.** Wind vectors over Alaska and northwestern Canada at 12 UT on 10 January 2010 (purple arrows). The pressure level is 500 mb, which corresponds to an altitude of  $\sim 5$  km. The length of each vector is proportional to the speed, which has a maximum value of 33.4 m/s. PFISR is shown as a red star. Areas with large mountains taller than  $\sim 2$ – $3$  km are shown as brown shading. (There are many mountains taller than 4 km in these areas.)

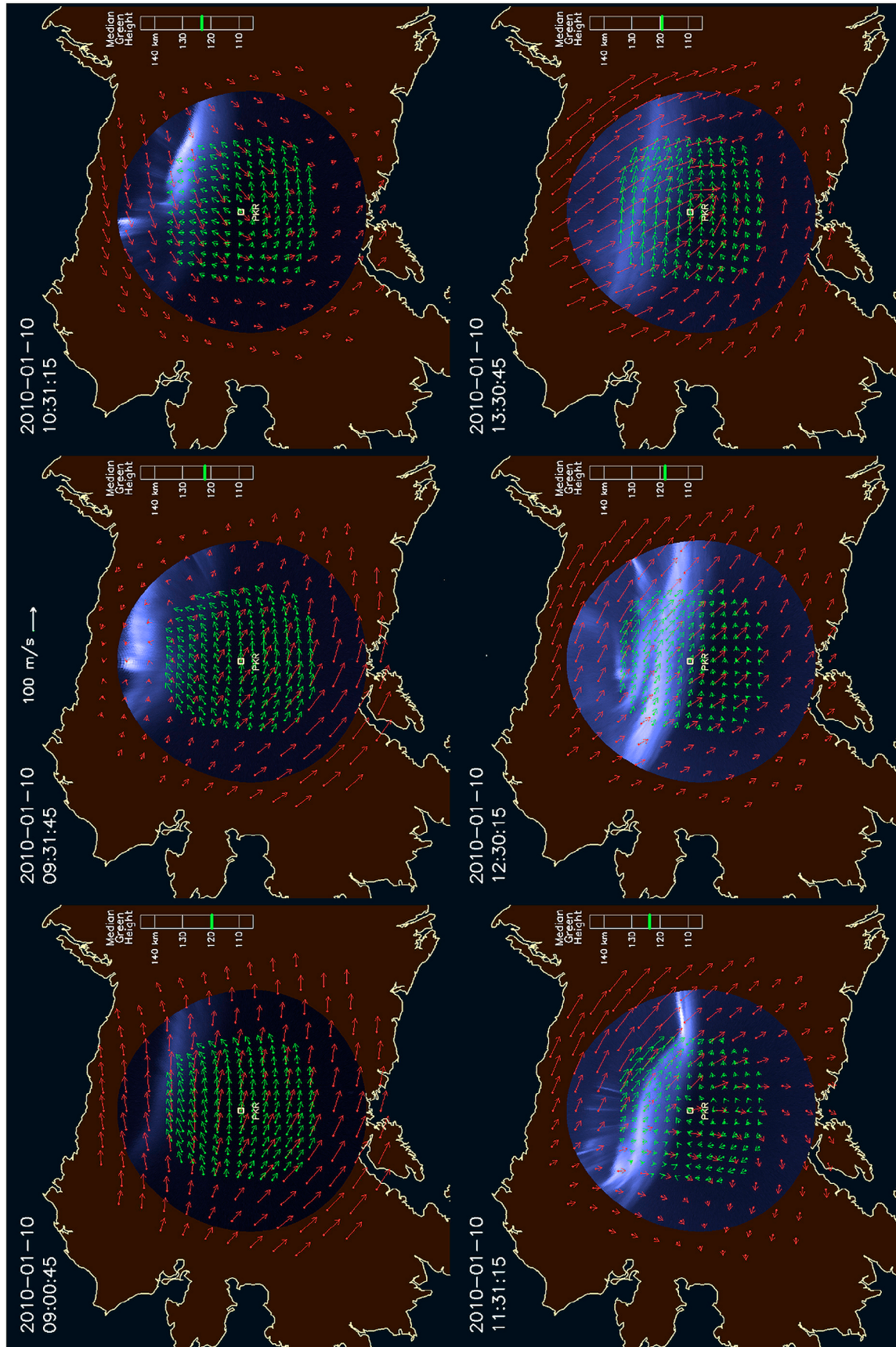


**Figure 14.** Six frames from 0930–1330 UT of combined measurements showing the Poker Flat SDI 630.0-nm *F*-region winds (red arrows) and 557.7-nm *E*-region winds (green arrows), as well as the 557.7-nm auroral emission intensity measured by a digital all-sky camera at Poker Flat (blue shading).

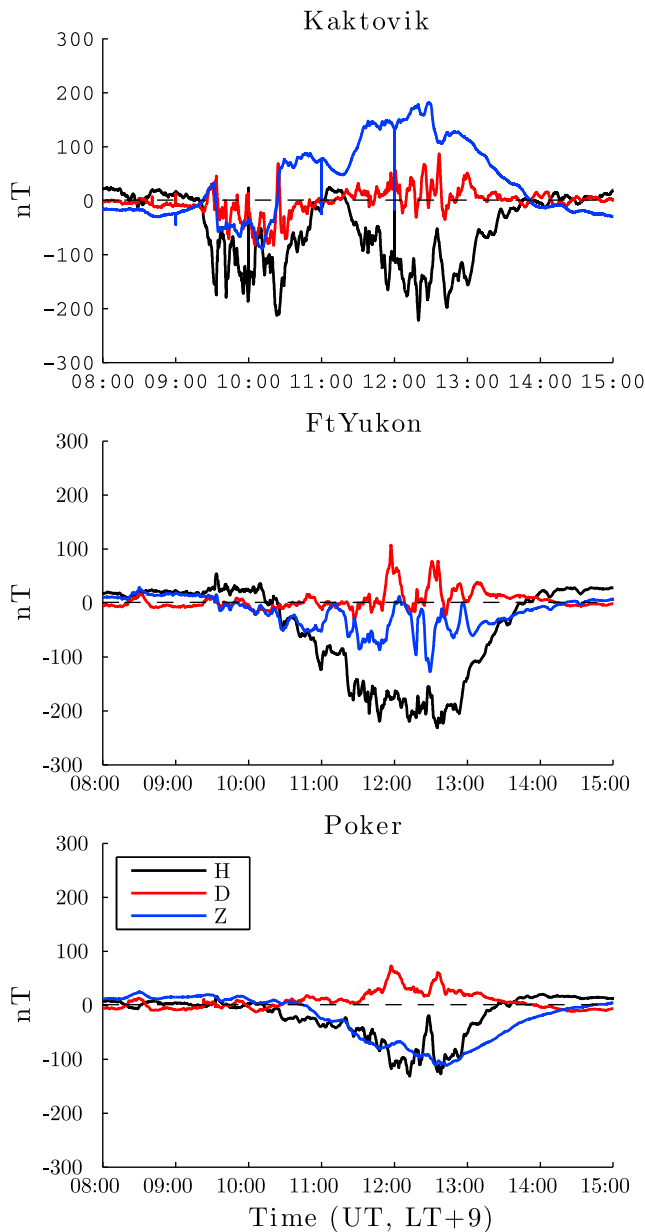


**Figure 15.** Magnetometer deflections from 8–15 UT on 10 January 2010 from 3 Alaska stations: Kaktovik ( $70.14^{\circ}\text{N}$ ), Ft. Yukon ( $66.56^{\circ}\text{N}$ ), and Poker Flat ( $65.12^{\circ}\text{N}$ ).

are fairly typical of aurorally generated waves [e.g., *Bristow et al.*, 1996].

[49] Figure 14 shows 6 frames of combined measurements from the Poker Flat SDI all-sky ( $\sim 200\text{--}300\text{-km}$ ) red and green-line ( $\sim 120\text{-km}$ ) neutral winds as well as frames from a digital all-sky camera at Poker Flat overlaid on a map of Alaska from 9–1330 UT. The auroral activity took place primarily to the north until an expansion toward the south began developing at around 1148 UT (2648 LT) (precise timing cannot be seen in these frames, which are plotted hourly). This auroral form reached zenith at Poker Flat at  $\sim 1201$  UT (2701 LT) and became very active over 20 minutes subsiding by 1250 UT (2750) LT. Pulsating auroral forms were observed during this time.

[50] Clear oscillations of the monochromatic GW were seen in the vertical velocity component after 2530 LT (see Figure 2b). Because this GW propagated northeastward, and because the aurora did not move south of Poker Flat until  $\sim 2648$  LT, auroral effects, such as Joule heating, that may have generated the GW must have been to the south of the dominant activity. Because height-resolved convection measurements were not available from PFISR on this night, we cannot evaluate the Joule heating rates to investigate this as a possible source. It is possible that Lorentz body-force acceleration created this GW [e.g., *Chimonas and Hines*, 1970; *Francis*, 1975; *Hunsucker*, 1977, 1982; *Jing and Hunsucker*, 1993] associated with the brightening of the auroral form. Further insight is gained by examining the magnetometer deflections, which are plotted in Figure 15 for three stations: from North to South, Kaktovik, Ft. Yukon, and Poker Flat. Auroral currents before 1030 UT were significant only well to the north of Poker Flat. After that time, as indicated by the negative  $H$  deflections, Ft. Yukon and Poker Flat were under the influence of the westward electrojet region. The generally positive  $Z$  values at Kaktovik, negative  $Z$  values at Poker Flat, and  $\sim$ zero-average  $Z$  values over Ft. Yukon indicate that the average location of the electrojet was near Ft. Yukon. Given that the magnetic deflections over Poker Flat began to increase around 1030 UT, around the time that the wave perturbations were initially seen by the FPI network, the GW may have been created by Lorentz forcing associated with auroral currents.

[51] Turning back to the wind measurements shown in Figure 14, another possibility for the generation of the GW is the rapid, large-scale changes in the background neutral wind field at both  $E$ - and  $F$ -region heights. The spatially resolved Poker Flat SDI measurements show that between 9 and 1030 UT, enhanced westward convection associated with pre-midnight ( $\sim 11$  UT) auroral flows was forcing the neutral winds to the north of Poker Flat westward at both  $E$ - and  $F$ -region heights. After magnetic midnight, the convection reversed, and the winds responded, so that the sense of the meridional shear in the (magnetic) zonal wind also reversed. This change in the wind field was fairly rapid and implies significant acceleration of the horizontal wind. The horizontal acceleration is analogous to a horizontal body force, the response to which depends both on the spatial and temporal extent of the forcing [*Vadas and Fritts*, 2001]. Determining whether the rapid changes in the wind field could have been the source of the observed GW activity would require modeling this neutral wind acceleration and assessing the characteristics of the excited GWs at the observation altitude.

[52] If the source were indeed auroral, the fact that the wave was observed to propagate northward may seem surprising given that most of the auroral activity was to the north of Poker Flat. However, there are several reasons why GWs generated by auroral activity to the north of Poker may not have been observed. Because the background winds were strongly southward (see Table 2 and Figure 3), southward propagating waves would have large intrinsic periods (if the observed GW were propagating southward with the same parameters, it would have  $\tau_{I_r} > \sim 45$  min). For example, for a source at  $z = 120$  km, Figure 4b of *Vadas* [2007] indicates that such a wave would have a fairly short

vertical wavelength ( $\sim 100$  km) and a dissipation altitude of 200–225 km. This would make these waves difficult / impossible to detect with the methods used in this paper. Such waves would have traveled  $\sim 750$  km horizontally and  $\sim 1$ – $1.5$  h prior to dissipating [see *Vadas, 2007, Figure 5b*]. In contrast, a northward propagating wave under these background wind conditions would propagate much more quickly (and with a smaller horizontal propagation distance) to the observation altitude. Finally, observations from the Dynamics Explorer 2 satellite have shown that the majority of the aurorally generated wave activity is observed to occur poleward of the nominal auroral oval [*Innis and Conde, 2002*], which seems to be consistent with this interpretation. Geometrical spreading may also contribute to differences in observability as waves propagate from their source.

## 5. Conclusions

[53] We have examined a  $\sim$ monochromatic GW with a 32-minute period detected by three FPI instruments in Alaska on 9–10 January 2010. The unique feature of these observations was that the LOS velocity, vertical velocity, and temperature perturbations of the GW were measured at multiple locations, thereby allowing for a detailed comparison with GW dissipative theory. We used a forward-fitting model applied to the LOS and vertical velocities in order to infer the following GW parameters: horizontal wavelength  $\lambda_H \sim 685$ – $1500$  km, propagation direction  $\theta = 17$ – $50^\circ$ , and horizontal phase speed  $c_H = 350$ – $770$  m/s. The northward propagation of the wave was confirmed by Poker Flat SDI observations. It was found that the phase shift/amplitude ratio between  $w'$ ,  $u'_H$ , and the temperature perturbation,  $T'$ , did not follow the conventional “Boussinesq” solutions, thereby implying that  $|\lambda_z| \gg H$  and/or that the GW was affected (to some extent) by viscosity. PFISR also observed this upward-propagating GW, from which an estimate and lower-bound of  $\lambda_z$  was obtained.

[54] We compared these observations and fitted results with GW dissipative theory. We found that we were able to find solutions within the range of the measurements, thereby validating the theory and its inherent assumptions (e.g., that the GW source is temporally and spatially localized, and that  $v$  can be assumed locally constant for the GW) for this one case. The “most likely” theoretical GW had  $\lambda_H = 750$  km,  $\lambda_z = -450$  km, and  $c_H = 390$  m/s, and was consistent with background parameters near the upper portion of the 630-nm emission layer.

[55] We also discussed possible sources of this GW. Since the GW most likely originated in the thermosphere, and given the observational coincidence with the time of enhanced auroral activity, the most likely sources include Joule heating, Lorentz forcing, wind shear, or induced body forcing of the horizontal wind by auroral convection, currents, and precipitation. A large-scale, fairly rapid (tens-of-minutes) reconfiguration of the background horizontal wind at both  $E$ - and  $F$ -region heights was observed by the Poker Flat SDI, which may have been induced by auroral convection and generated the observed GW. While most of the auroral activity and dynamics occurred to the north of Poker Flat, the background wind conditions favored northward-propagating GWs, consistent with the observations. Finally, since there were large winds in the mountains 400–500 km

south of Poker Flat, we cannot rule out the possibility that this GW may have been a tertiary GW excited by the dissipation of secondary GWs created by mountain-wave breaking.

[56] These observations and results show that multiple, high-resolution FPI instruments can be used to observe individual GWs in the thermosphere. Forward modeling can then be used to determine their parameters. The GW dissipative theory derived in the companion paper can then be used to infer unmeasured parameters (such as  $\lambda_z$ ). Additional measurements from co-located instruments sensitive to neutral parameters (such as all-sky imaging FPI systems) and/or able to measure range-resolved parameters (such as incoherent scatter radars) are useful for confirming derived wave properties and investigating wave sources.

[57] **Acknowledgments.** The authors acknowledge Patrice Sutter for providing Figure 13. MJN was supported by NSF grant AGS-0836142. PFISR data collection and analysis was supported by NSF cooperative agreement AGS-0608577 to SRI International. SLV was supported by NSF grant ATM-0836195, and NASA contracts NNNH08CE12C and NNNH10CC98C. JWM was supported by NSF grant AGS-0640641. DH was supported by NSF grant ATM-0608577. Poker Flat SDI data collection and analysis were supported under NSF grant ATM-0737618 to the Geophysical Institute of the University of Alaska Fairbanks.

[58] Robert Lysak thanks the reviewers for their assistance in evaluating this paper.

## References

- Aruliah, A. L., and D. Rees (1995), The trouble with thermospheric vertical winds: Geomagnetic, seasonal and solar cycle dependence at high latitudes, *J. Atmos. Terr. Phys.*, *57*, 597–609.
- Aruliah, A. L., et al. (2005), First direct evidence of meso-scale variability on ion-neutral dynamics using co-located tristatic FPIs and EISCAT radar in Northern Scandinavia, *Ann. Geophys.*, *23*, 147–162, doi:10.5194/angeo-23-147-2005.
- Aruliah, A. L., E. M. Griffin, H.-C. I. Yiu, I. McWhirter, and A. Charalambous (2010), SCANDI – an all-sky Doppler imager for studies of thermospheric spatial structure, *Ann. Geophys.*, *28*, 549–567, doi:10.5194/angeo-28-549-2010.
- Bauer, S. J. (1958), An apparent ionospheric response to the passage of hurricanes, *J. Geophys. Res.*, *63*, 265–269, doi:10.1029/JZ063i001p00265.
- Bishop, R. L., N. Aponte, G. D. Earle, M. Sulzer, M. F. Larsen, and G. S. Peng (2006), Arecibo observations of ionospheric perturbations associated with the passage of Tropical Storm Odette, *J. Geophys. Res.*, *111*, A11320, doi:10.1029/2006JA011668.
- Bristow, W. A., R. A. Greenwald, and J. P. Villain (1996), On the seasonal dependence of medium-scale atmospheric gravity waves in the upper atmosphere at high latitudes, *J. Geophys. Res.*, *101*, 15,685–15,700, doi:10.1029/96JA01010.
- Bruinsma, S. L., and J. M. Forbes (2009), Properties of traveling atmospheric disturbances (TADs) inferred from CHAMP accelerometer observations, *Adv. Space Res.*, *43*, 369–376, doi:10.1016/j.asr.2008.10.031.
- Chimonas, G., and C. O. Hines (1970), Atmospheric gravity waves launched by auroral currents, *Planet. Space Sci.*, *18*, 565–582.
- Chimonas, G., and W. R. Peltier (1970), The bow wave generated by an auroral arc in supersonic motion, *Planet. Space Sci.*, *18*, 599–612.
- Conde, M., and R. W. Smith (1995), Mapping thermospheric winds in the auroral zone, *Geophys. Res. Lett.*, *22*, 3019–3022, doi:10.1029/95GL02437.
- Conde, M., and R. W. Smith (1997), Phase compensation of a separation scanned, all-sky imaging Fabry-Perot spectrometer for auroral studies, *Appl. Opt.*, *36*, 5441–5450.
- Conde, M., and R. W. Smith (1998), Spatial structure in the thermospheric horizontal wind above Poker Flat, Alaska, during solar minimum, *J. Geophys. Res.*, *103*, 9449–9471.
- Conde, M., et al. (2001), Assimilated observations of thermospheric winds, the aurora, and ionospheric currents over Alaska, *J. Geophys. Res.*, *106*, 10,493–10,508, doi:10.1029/2000JA000135.
- Conde, M. G., and M. J. Nicolls (2010), Thermospheric temperatures above Poker Flat, Alaska, during the stratospheric warming event of January and February 2009, *J. Geophys. Res.*, *115*, D00N05, doi:10.1029/2010JD014280.
- Djuth, F. T., M. P. Sulzer, J. H. Elder, and V. B. Wickwar (1997), High-resolution studies of atmosphere-ionosphere coupling at Arecibo Observatory, Puerto Rico, *Radio Sci.*, *32*, 2321–2344, doi:10.1029/97RS02797.

- Djuth, F. T., M. P. Sulzer, S. A. Gonz ales, J. D. Mathews, J. H. Elder, and R. L. Walterscheid (2004), A continuum of gravity waves in the Arecibo thermosphere?, *Geophys. Res. Lett.*, *31*, L16801, doi:10.1029/2003GL019376.
- Ford, E. A. K., A. L. Aruliah, E. M. Griffin, and I. McWhirter (2006), Thermospheric gravity waves in Fabry-Perot Interferometer measurements of the 630.0nm OI line, *Ann. Geophys.*, *24*, 555–566, doi:10.5194/angeo-24-555-2006.
- Ford, E. A. K., A. L. Aruliah, E. M. Griffin, and I. McWhirter (2008), Statistical analysis of thermospheric gravity waves from Fabry-Perot Interferometer measurements of atomic oxygen, *Ann. Geophys.*, *26*, 29–45, doi:10.5194/angeo-26-29-2008.
- Francis, S. H. (1973), Acoustic-gravity modes and large-scale traveling ionospheric disturbances of a realistic, dissipative atmosphere, *J. Geophys. Res.*, *78*, 2278–2301, doi:10.1029/JA078i013p02278.
- Francis, S. H. (1975), Global propagation of atmospheric gravity waves: A review, *J. Atmos. Terr. Phys.*, *37*, 1011–1030.
- Fritts, D. C., and M. J. Alexander (2003), Gravity wave dynamics and effects in the middle atmosphere, *Rev. Geophys.*, *41*(1), 1003, doi:10.1029/2001RG000106.
- Fritts, D. C., and S. L. Vadas (2008), Gravity wave penetration into the thermosphere: sensitivity to solar cycle variations and mean winds, *Ann. Geophys.*, *26*, 3841–3861, doi:10.5194/angeo-26-3841-2008.
- Georges, T. M. (1968), HF Doppler studies of traveling ionospheric disturbances, *J. Atmos. Terr. Phys.*, *30*, 735–746.
- Hajkowicz, L. A. (1990), A global study of large scale travelling ionospheric disturbances (TIDS) following a step-like onset of auroral substorms in both hemispheres, *Planet. Space Sci.*, *38*, 913–923.
- Herrero, F. A., H. G. Mayr, I. Harris, F. Varosi, and J. W. Meriwether (1984), Thermospheric gravity waves near the source: Comparison of variations in neutral temperature and vertical velocity at Sonore Stromfjord, *Geophys. Res. Lett.*, *11*(9), 939–942, doi:10.1029/GL011i009p00939.
- Hines, C. O. (1960), Internal atmospheric gravity waves at ionospheric heights, *Can. J. Phys.*, *38*, 1441–1481.
- Hocke, K., and K. Schlegel (1996), A review of atmospheric gravity waves and travelling ionospheric disturbances: 1982–1995, *Ann. Geophys.*, *14*, 917–940.
- Hocke, K., and T. Tsuda (2001), Gravity waves and ionospheric irregularities over tropical convection zones observed by GPS/MET radio occultation, *Geophys. Res. Lett.*, *28*, 2815–2818, doi:10.1029/2001GL013076.
- Hung, R. J., and J. P. Kuo (1978), Ionospheric observation of gravity-waves associated with hurricane Eloise, *J. Geophys. Res.*, *45*, 67–80.
- Hunsucker, R. D. (1977), Estimate of the relative importance of Joule heating and the Lorentz force in generating atmospheric gravity waves from the auroral electrojet, *J. Geophys. Res.*, *82*, 4826–4828, doi:10.1029/JA082i029p04826.
- Hunsucker, R. D. (1982), Atmospheric gravity waves generated in the high-latitude ionosphere: A review, *Rev. Geophys.*, *20*, 293–315.
- Innis, J. L., and M. Conde (2002), High-latitude thermospheric vertical wind activity from Dynamics Explorer 2 Wind and Temperature Spectrometer observations: Indications of a source region for polar cap gravity waves, *J. Geophys. Res.*, *107*(A8), 1172, doi:10.1029/2001JA009130.
- Innis, J. L., P. L. Dyson, and P. A. Greet (1997), Further observations of the thermospheric vertical wind at the auroral oval/polar cap boundary, *J. Atmos. Sol. Terr. Phys.*, *59*, 2009–2022.
- Jing, N., and R. D. Hunsucker (1993), A theoretical investigation of sources of large and medium scale atmospheric gravity waves in the auroral oval, *J. Atmos. Terr. Phys.*, *55*, 1667–1679.
- Kelley, M. C. (1997), In situ ionospheric observations of severe weather-related gravity waves and associated small-scale plasma structure, *J. Geophys. Res.*, *102*, 329–336, doi:10.1029/96JA03033.
- Laštovička, J. (2006), Forcing of the ionosphere by waves from below, *J. Atmos. Sol. Terr. Phys.*, *68*, 479–497, doi:10.1016/j.jastp.2005.01.018.
- Makela, J. J., J. W. Meriwether, Y. Huang, and P. Sherwood (2011), Simulation and analysis of a multi-order imaging Fabry-Perot interferometer for the study of thermospheric winds and temperatures, *Appl. Opt.*, *50*, 4403–4416.
- Mayr, H. G., I. Harris, F. A. Herrero, and F. Varosi (1984a), Global excitation of wave phenomena in a dissipative multiconstituent medium: 1. Transfer function of the Earth's thermosphere, *J. Geophys. Res.*, *89*, 10,929–10,959.
- Mayr, H. G., I. Harris, F. A. Herrero, and F. Varosi (1984b), Global excitation of wave phenomena in a dissipative multiconstituent medium: 2. Impulsive Perturbations in the Earth's thermosphere, *J. Geophys. Res.*, *89*, 10,961–10,986.
- Mayr, H. G., I. Harris, F. Varosi, and F. A. Herrero (1987), Global excitation of wave phenomena in a dissipative multiconstituent medium: 3. Response characteristics for different sources in the Earth's thermosphere, *J. Geophys. Res.*, *92*, 7657–7672.
- Mayr, H. G., I. Harris, F. A. Herrero, N. W. Spencer, F. Varosi, and W. D. Pesnell (1990), Thermospheric gravity waves - Observations and interpretation using the transfer function model (TFM), *Space Sci. Rev.*, *54*, 297–375.
- Meriwether, J. W., J. J. Makela, Y. Huang, D. J. Fisher, R. A. Burti, A. F. Medeiros, and H. Takahashi (2011), Climatology of the nighttime equatorial thermospheric winds and temperatures over Brazil near solar minimum, *J. Geophys. Res.*, *116*, A04322, doi:10.1029/2011JA016477.
- Nagy, A. F., R. J. Cicerone, P. B. Hays, K. D. McWatters, J. W. Meriwether, A. E. Belon, and C. L. Rino (1974), Simultaneous measurement of ion and neutral motions by radar and optical techniques, *Radio Sci.*, *9*, 315–321, doi:10.1029/RS009i002p00315.
- Nicolls, M. J., and C. J. Heinselman (2007), Three-dimensional measurements of traveling ionospheric disturbances with the Poker Flat Incoherent Scatter Radar, *Geophys. Res. Lett.*, *34*, L21104, doi:10.1029/2007GL031506.
- Nicolls, M. J., M. C. Kelley, A. J. Coster, S. A. Gonz ales, and J. J. Makela (2004), Imaging the structure of a large-scale TID using ISR and TEC data, *Geophys. Res. Lett.*, *31*, L09812, doi:10.1029/2004GL019797.
- Nicolls, M. J., R. H. Varney, S. L. Vadas, P. A. Stamus, C. J. Heinselman, R. B. Cosgrove, and M. C. Kelley (2010), Influence of an inertia-gravity wave on mesospheric dynamics: A case study with the Poker Flat Incoherent Scatter Radar, *J. Geophys. Res.*, *115*, D00N02, doi:10.1029/2010JD014042.
- Oliver, W. L., Y. Otsuka, M. Sato, T. Takami, and S. Fukao (1997), A climatology of F region gravity wave propagation over the middle and upper atmosphere radar, *J. Geophys. Res.*, *102*, 14,499–14,512, doi:10.1029/97JA00491.
- Picone, J. M., A. E. Hedin, D. P. Drob, and A. C. Aikin (2002), NRLMSISE-00 empirical model of the atmosphere: Statistical comparisons and scientific issues, *J. Geophys. Res.*, *107*(A12), 1468, doi:10.1029/2002JA009430.
- Richmond, A. D. (1978), Gravity wave generation, propagation, and dissipation in the thermosphere, *J. Geophys. Res.*, *83*, 4131–4145, doi:10.1029/JA083iA09p04131.
- Rishbeth, H. (1972), Thermospheric winds and the F-region: A review, *J. Atmos. Terr. Phys.*, *34*, 1–47.
- Roettger, J. (1977), Travelling disturbances in the equatorial ionosphere and their association with penetrative cumulus convection, *J. Atmos. Terr. Phys.*, *39*, 987–998.
- Sica, R. J., G. Hernandez, G. J. Romick, M. H. Rees, and R. G. Roble (1986a), Auroral zone thermospheric dynamics: 2. Individual nights, *J. Geophys. Res.*, *91*, 13,593–13,611, doi:10.1029/JA091iA12p13593.
- Sica, R. J., M. H. Rees, G. J. Romick, G. Hernandez, and R. G. Roble (1986b), Auroral zone thermospheric dynamics: 1. Averages, *J. Geophys. Res.*, *91*, 3231–3244, doi:10.1029/JA091iA03p03231.
- Smith, R. W. (1998), Vertical winds: a tutorial, *J. Atmos. Sol. Terr. Phys.*, *60*, 1425–1434.
- Tsugawa, T., A. Saito, Y. Otsuka, and M. Yamamoto (2003), Damping of large-scale traveling ionospheric disturbances detected with GPS networks during the geomagnetic storm, *J. Geophys. Res.*, *108*(A3), 1127, doi:10.1029/2002JA009433.
- Vadas, S. L. (2007), Horizontal and vertical propagation and dissipation of gravity waves in the thermosphere from lower atmospheric and thermospheric sources, *J. Geophys. Res.*, *112*, A06305, doi:10.1029/2006JA011845.
- Vadas, S. L., and D. C. Fritts (2001), Gravity wave radiation and mean responses to local body forces in the atmosphere, *J. Atmos. Sci.*, *58*, 2249–2279.
- Vadas, S. L., and H.-L. Liu (2009), Generation of large-scale gravity waves and neutral winds in the thermosphere from the dissipation of convectively generated gravity waves, *J. Geophys. Res.*, *114*, A10310, doi:10.1029/2009JA014108.
- Vadas, S. L., and H.-L. Liu (2011), Neutral winds and densities at the bottomside of the F layer from primary and secondary gravity waves from deep convection, in *Aeronomy of the Earth's Atmosphere and Ionosphere, IAGA Spec. Sopron Book Ser.*, vol. 2, pp. 131–139, Springer, New York.
- Vadas, S. L., and M. J. Nicolls (2008), Using PFISR measurements and gravity wave dissipative theory to determine the neutral, background thermospheric winds, *Geophys. Res. Lett.*, *35*, L02105, doi:10.1029/2007GL031522.
- Vadas, S. L., and M. J. Nicolls (2009), Temporal evolution of neutral, thermospheric winds and plasma response using PFISR measurements of gravity waves, *J. Atmos. Sol. Terr. Phys.*, *71*, 744–770, doi:10.1016/j.jastp.2009.01.011.
- Vadas, S. L., and M. J. Nicolls (2012), The phases and amplitudes of gravity waves propagating and dissipating in the thermosphere: Theory, *J. Geophys. Res.*, *117*, A05322, doi:10.1029/2011JA017426.

- Vadas, S. L., D. C. Fritts, and M. J. Alexander (2003), Mechanism for the generation of secondary waves in wave breaking regions, *J. Atmos. Sci.*, *60*, 194–214.
- Vadas, S. L., et al. (2009), Convection: The likely source of the medium-scale gravity waves observed in the OH airglow layer near Brasilia, Brazil, during the SpreadFEX campaign, *Ann. Geophys.*, *27*, 231–259, doi:10.5194/angeo-27-231-2009.
- Waldock, J. A., and T. B. Jones (1987), Source regions of medium scale travelling ionospheric disturbances observed at mid-latitudes, *J. Atmos. Terr. Phys.*, *49*, 105–114.
- Walterscheid, R. L., L. R. Lyons, and K. E. Taylor (1985), The perturbed neutral circulation in the vicinity of a symmetric stable auroral arc, *J. Geophys. Res.*, *90*, 12,235–12,248.
- Yeh, K. C., and C. H. Liu (1974), Acoustic-gravity waves in the upper atmosphere, *Rev. Geophys.*, *12*, 193–216.
- Yiğit, E., and A. S. Medvedev (2010), Internal gravity waves in the thermosphere during low and high solar activity: Simulation study, *J. Geophys. Res.*, *115*, A00G02, doi:10.1029/2009JA015106.